Università degli Studi di Padova

Department of Physics and Astronomy

Master Thesis in Physics

Signal Formation in the new Time Projection Chambers of the T2K Upgraded Experiment

Supervisor
Prof. Gianmaria Collazuol
Università degli Studi di Padova

Co-supervisor
Dr. Magda Cicerchia
Istituto Nazionale di Fisica Nucleare
Laboratori Nazionali di Legnaro

Master Candidate
dott. Luca Scomparin

Abstract

The goal of the T2K experiment is to obtain new insights on the phenomena of neutrino oscillations. In order to improve the near detector of the experiment an upgrade is planned, with the addition, among other detectors, of two HA-TPCs (High Angle Time Projection Chambers). The use of MICROMEGAS with an additional resistive layer (ERAM) adds an effect of charge spread, enabling higher resolution for a fixed number of electronic channels and improved spark protection.

The scope of this thesis is to gain a better understanding of the physics of charge spread and a detailed signal formation description. A finite element simulation is developed, allowing to validate analytical models of this phenomena. Moreover, the previously unaccounted for effect of the ion drift in the amplification gap is studied. A method exploiting a complete model of signal formation, together with the response of the electronic front-end, is proposed for the characterization of the acquired pad signals, serving as a starting point for future calibrations and analyses.

Additionally, the installation and setup of the HA-TPC prototype for a test beam at the DESY laboratory in Hamburg is reported, together with the application of the aforementioned analysis method to the early data collected.

Sommario

L'obiettivo dell'esperimento T2K è l'avanzamento della comprensione del fenomeno delle oscillazioni dei neutrini. Per migliorare le caratteristiche del rivelatore vicino ne è stato pianificato un aggiornamento che prevede l'installazione, oltre ad altri rivelatori, di due camere a proiezione temporale ad alto angolo (HA-TPC). L'uso di MICROMEGAS con l'aggiunta di uno strato resistivo introduce un effetto di diffusione della carica che permette di ottenere una maggiore risoluzione, a parità di numero di canali di elettronica, migliorandone inoltre la protezione dalle scariche.

La finalità di questa tesi è ottenere una più completa comprensione della fisica della diffusione della carica e descrivere dettagliatamente la formazione del segnale. Una simulazione agli elementi finiti è stata sviluppata, permettendo la validazione dei modelli analitici di questo fenomeno. In seguito è stato studiato l'effetto del moto di deriva degli ioni nello strato di amplificazione, finora mai considerato. È poi stato proposto un metodo che sfrutta un modello completo di formazione del segnale e della risposta dell'elettronica di front-end, utilizzabile per la caratterizzazione del segnale acquisito da ogni pad e che potrà servire come punto di partenza per future calibrazioni e analisi.

In aggiunta si descrive la preparazione e l'installazione del prototipo della HA-TPC per un test beam ai laboratori di DESY, ad Amburgo. La procedura di analisi descritta precedentemente è stata poi applicata ai dati appena ottenuti.

Contents

1

An introduction to neutrino oscillations

1.1 Discrete symmetries

A physical theory might possess a number of discrete symmetries, representing the invariance under noncontinuous transformations. The main examples of such symmetries are the well-known P, C, and T. The first one represents the invariance under parity transformations, i.e., the inversion of spatial coordinates. The second one is the invariance under charge conjugation, i.e. the inversion of all particles' charges. The last one is the invariance under time inversion.

At first it was thought that physical theories were invariant under all of them. In 1956, though, Wu showed that weak interactions violate parity [1] *. A new symmetry was then proposed, the so called CP symmetry, specifically the invariance under a spatial inversion and the inversion of all particle's charges. This is equivalent to exchanging particles with antiparticles. Later, in 1964, searches of forbidden decays in neutral kaons showed [3] that even this symmetry is violated by weak interactions. Such an effect in the quark sector is known today in a variety of other systems, including B_0 oscillations.

It is still unknown whether such a violation is also characteristic of the leptonic sector. This search is the physical case of study of this work of thesis. To understand it better, a brief introduction to neutrino oscillations is necessary.

*Except where otherwise stated a general reference for this chapter is [2].

1.2 A TOY MODEL OF NEUTRINO OSCILLATIONS

A well established phenomena in neutrino physics are the so-called neutrino oscillations[4, 5, 6]. This effect arises only in the case of massive neutrinos where their flavor and mass eigenstates do not coincide. In layman terms this is equivalent to saying that a neutrino is produced and interacts in a well defined flavor state, i.e. like an electron, muon or tau neutrino, but it undergoes propagation as a superposition of mass states. Mathematically, a given flavor state can be written as a linear combination of mass states

$$|\nu_\alpha\rangle = \sum_i U^*_{\alpha i} |\nu_i\rangle$$

where $U_{\alpha i}$ are the elements of the unitary mixing matrix. In the following treatment the flavor states will be written with greek letter indices, while the mass states will use latin letters.

To better understand this abstract statement the classic example is the study of a system with only two neutrinos having masses m_1 and m_2. The neutrino state can be written in two different basis: the interaction one, where it has a defined flavor, and the hamiltonian one, where it has a defined mass. Due to the fact that the mixing matrix has to be unitary, it can be written in the two-dimensional case as a simple rotation matrix of an angle θ

$$U = \begin{pmatrix} \cos\theta & -\sin\theta \\ \sin\theta & \cos\theta \end{pmatrix}$$

By using this mixing matrix parametrization an electron neutrino state can be written as

$$|\nu_e\rangle = \cos\theta\,|\nu_1\rangle - \sin\theta\,|\nu_2\rangle$$

By definition, the mass basis is an eigenstate of the hamiltonian matrix, so the vector above evolves in time as

$$|\nu_e(t)\rangle = \cos\theta e^{-iE_1 t}\,|\nu_1\rangle - \sin\theta e^{-iE_2 t}\,|\nu_2\rangle$$

Using the assumption that neutrino have a small mass compared to their energy, the energy of an eigenstate can be written using the ultrarelativistic approximation as a function of the neutrino energy E

$$E_i = \sqrt{p^2 + m_i^2} \approx p + \frac{m_i^2}{2p} \approx E + \frac{m_i^2}{2E}$$

It is now possible to calculate the probability that a neutrino that at $t = 0$ was in an electron flavor state will still be in that state after a time t

$$P_{e\to e}(t) = |\,\langle \nu_e | \nu_e(t) \rangle\,|^2 = 1 - \sin^2 2\theta \, \sin^2 \frac{\Delta m^2 \, L}{4E} \neq 1$$

where in natural units $L = t$ and $\Delta m^2 \equiv m_1^2 - m_2^2$.

This toy model shows that due to their different mass, the hamiltonian eigenstates obtain a relative phase during their time evolution, resulting in a mixing of the flavor states that produces the oscillation.

1.3 The $N = 3$ case

In case of two neutrinos the mixing matrix can be written concisely with just one parameter, namely the mixing angle. Experimental evidence shows that the actual number of neutrinos is three. In this case, though, the number of parameters of the mixing matrix is four, three mixing angles and one phase[†]. A common parametrization is the following

$$U = \begin{pmatrix} 1 & 0 & 0 \\ 0 & c_{23} & s_{23} \\ 0 & -s_{23} & c_{23} \end{pmatrix} \begin{pmatrix} c_{13} & 0 & s_{13}e^{-i\delta} \\ 0 & 1 & 0 \\ -s_{13}e^{i\delta} & 0 & c_{13} \end{pmatrix} \begin{pmatrix} c_{12} & s_{12} & 0 \\ -s_{12} & c_{12} & 0 \\ 0 & 0 & 1 \end{pmatrix}$$

where the sine and cosine of the three mixing angles θ_{23}, θ_{13} and θ_{12} were abbreviated as $c_{ij} = \cos\theta_{ij}$ and $s_{ij} = \sin\theta_{ij}$. The phase term δ is currently unknown. This mixing matrix is called the Pontecorvo-Maki-Nakagawa-Sakata (PMNS) matrix.

1.4 The CP violating phase

It can be shown that the δ phase of the PMNS matrix can produce CP violation. In order to have a parametrization independent measure of such violation the Jarlskog invariant is introduced

$$\begin{aligned} J &\equiv J_{\text{CP}}^{\max} \sin\delta \\ &= \cos\theta_{12} \sin\theta_{12} \cos\theta_{23} \sin\theta_{23} \cos^2\theta_{13} \sin\theta_{13} \sin\delta \end{aligned}$$

[†]Precisely there are two additional Majorana phases that will not be treated here because they do not affect the oscillations.

This observable clearly depends on both the mixing angles and the phase. A non-zero phase might not lead to CP violation if any of the mixing angles is zero. Moreover if all the mixing angles are non-zero, and experimentally this is actually the case, the sine of the phase still needs to be non-zero.

This potential non-zero value would have a strong impact on the cosmological models trying to explain the several orders of magnitude discrepancy among the observed matter-antimatter asymmetry and the one predicted by the Standard Model (SM) of particle physics. In fact a known source of this asymmetry comes from the CP violation in the quark sector. This, though, is not sufficiently large to explain the current observations.

Moreover, the neutrino sector has the potential to show a violation several orders of magnitude greater than the quark sector one. In complete analogy to the neutrino PMNS matrix, in the quark sector there is the Cabibbo-Kobayashi-Maskawa (CKM) matrix. Although they are equivalent they exibith a very different structure. The CKM matrix is nearly diagonal with small non-diagonal elements (i.e. small mixing angles). In the CKM matrix $J \approx 3 \times 10^{-5}$ with a great phase angle of the order of $68°$. So, the small Jarlskog invariant is mainly due to the smallness of the mixing angles, and not to a small phase.

In the PMNS matrix, on the other hand, there is a very different structure with two large mixing angles. If the maximum possible value of J is computed, the value is of the order of $J_{\text{CP}}^{\text{max}} \approx 3 \times 10^{-2}$. This sizable difference might lead to an effect several orders of magnitude greater than the one observed in the quark sector.

1.5 CP violation in neutrino oscillation

A calculation of the oscillation probability analogous to the one shown in section 1.2 can be performed in the general case as a function of the PMNS matrix elements and the square difference of masses, leading to

$$\begin{aligned} P_{\alpha\beta} = \delta_{\alpha\beta} - 4 \sum_{i<j}^{n} \Re \left[U_{\alpha i} U_{\beta i}^{*} U_{\alpha j}^{*} U_{\beta j} \right] \sin^2 X_{ij} \\ + 2 \sum_{i<j}^{n} \Im \left[U_{\alpha i} U_{\beta i}^{*} U_{\alpha j}^{*} U_{\beta j} \right] \sin 2X_{ij} \end{aligned}$$

where $P_{\alpha\beta}$ is the probability to find a neutrino of energy E initially of flavor β in flavor α after a distance L, with $X_{ij} \equiv (m_i^2 - m_j^2)L/(4E)$. $\Re[z]$ and $\Im[z]$ are respectively the real

and imaginary parts of a complex number z.

The CP transformed version of the above is the probability to find an **anti**neutrino initially of flavor β in flavor α. This is equivalent to substituting U with U^* (and vice-versa) in the above expression. It is clear that the first line is left unchanged, while the second line gets a minus sign.

At this point, the probability asymmetry is defined as

$$\begin{aligned} A_{\alpha\beta} &= P_{\alpha\beta} - P_{\bar{\alpha}\bar{\beta}} \\ &= 4 \sum_{i<j}^{n} \Im \left[U_{\alpha i} U_{\beta i}^* U_{\alpha j}^* U_{\beta j} \right] \sin 2X_{ij} \end{aligned}$$

This formula is important because it allows to see which kind of oscillation experiments are sensitive to CP violation. For example, consider a survival experiment where the measurement of probability that a neutrino of flavor α is still in that flavor after the oscillation is performed. Evaluating the probability asymmetry in such a case gives

$$\begin{aligned} A_{\alpha\alpha} &= 4 \sum_{i<j}^{n} \Im \left[U_{\alpha i} U_{\alpha i}^* U_{\alpha j}^* U_{\alpha j} \right] \sin 2X_{ij} \\ &= 4 \sum_{i<j}^{n} \Im \left[|U_{\alpha i}|^2 |U_{\alpha j}|^2 \right] \sin 2X_{ij} \\ &= 0 \end{aligned}$$

because, being the modulus squared always real, its imaginary part is zero. This shows that no difference can be observed in such survival experiment.

Therefore, the only kind of experiment that might give information on CP violation in this sector are appearance experiments, where the appearance of neutrinos of a different flavor in an oscillated neutrino beam is measured.

1.6 Matter effects and neutrino mass hierarchy

As shown in the previous sections neutrino oscillation are sensitive only to the difference of squared masses. Thus, oscillations cannot give us information on the absolute mass scale, nor

on the ordering of the mass eigenstates. This is true, though, only in the case where neutrinos are propagating in a vacuum. In fact, matter contains a great number of electrons. The interaction of neutrinos with electrons can happen in two different ways, namely charged current (CC) interactions and neutral current (NC) interactions. NC interaction is flavor blind, thus is equal for all neutrinos. CC interaction, on the other hand, affects only electron neutrinos. Thus, the hamiltonian must be modified by adding a potential energy term only to the electron neutrino state (in the flavor basis this matrix is not diagonal)

$$H = \begin{pmatrix} \sqrt{2}G_F n_e & 0 & 0 \\ 0 & 0 & 0 \\ 0 & 0 & 0 \end{pmatrix} + \frac{1}{2E} U \begin{pmatrix} m_1^2 & 0 & 0 \\ 0 & m_2^2 & 0 \\ 0 & 0 & m_3^2 \end{pmatrix} U^\dagger$$

where G_F is the Fermi constant, n_e is the electron density per unit volume and U is the PMNS matrix.

This additional term allows to obtain information on the ordering of the mass eigenstates. When the formulas of the previous section are corrected to take into account this kind of effects, the experiment gains sensitivity also to this additional physical observable.

2

The T2K experiment

The T2K (Tokai to Kamioka) experiment is a long baseline neutrino experiment located in Japan designed to search for CP violation effects in the neutrino sector and to perform measurements of neutrino oscillation parameters. The main idea is to produce a beam of muonic neutrinos and then detect the presence of electron neutrinos after a known distance (295 km), observing if the oscillation occurs. The ν beam energy is centered around 0.6 GeV, in order to have the maximum of oscillation probability at the far detector distance. *

The experiment comprises a production facility, several near detectors for the characterization of the ν beam, and a far detector for the study of the oscillated beam.

2.1 The Super-Kamiokande far detector

SK (Super-Kamiokande) is a well known detector in neutrino physics, thanks to its discovery of atmospheric neutrino oscillation and the detection of supernova neutrinos. Additionally it serves as the far detector for the T2K experiment.

SK is a cylindrical water Cherenkov detector located 1 km inside of Mount Ikenoyama, consisting of an active volume of 50 kt of ultrapure water read by roughly 13000 PMTs (PhotoMultiplier Tubes). It is divided into two parts: an inner and an outer detector. The latter serves as a veto to remove cosmic muons and events that are not fully contained in the

*A general reference for this chapter is [7] for T2K and [8] for the upgrade.

inner detector. When a neutrino interacts with water it can produce charged particles that might have a velocity greater than the speed of light in water. In this case they produce a cone of Cherenkov light that is detected by the PMTs. In order to measure the flavor composition of the incoming beam, only charged current interaction events are used, specifically CCQE (Charged Current Quasi-Elastic). In such an event the corresponding lepton is produced allowing the tag of the neutrino thanks to the SK PID (Particle IDentification) algorithms. Such analysis are based on the fact that, due to the lower electron mass compared to muons, they are scattered more, thus travelling in a less straight path in this way producing a fuzzier light ring.

An important aspect is that SK does not posses the ability to differentiate leptons from their antiparticle, i.e. it is not possible to distinguish μ^+ from μ^- and similarly for electrons. Thus, the level of wrong sign contamination has to be studied in some other way. In the T2K experiment this is done using another detector in the vicinity of the beam production site.

2.2 Beam production

Before discussing how the beam is characterized, this section explains how the neutrino beam is produced. A proton beam is extracted from the the MR (Main Ring) synchrothron at an energy of $30\ \mathrm{GeV}$ after it was accelerated to $3\ \mathrm{GeV}$ by the RCS (Rapid Cycling Synchrothron) and at $181\ \mathrm{MeV}$ by the LINAC (LINear ACcelerator). This spill, containing about 3×10^{14} protons, impinges on the helium-cooled target composed of a graphite rod about $90\ \mathrm{cm}$ long with a diameter of $2.6\ \mathrm{cm}$. Here a variety of particles are produced, the one of interest for the production of neutrinos are pions. Three magnetic horns following the target focalize the pions and, by inverting their current, allow the selection of either a positive or negative pions enriched beam. Then, the pion enter a $96\ \mathrm{m}$ long decay volume. Here they decay mainly into a muon and the corresponding neutrino, while the undecayed particles are stopped by a beam dump. The selection of negative or positive pion enriched beam allows the production of respectively an antineutrino or a neutrino enriched beam.

An important aspect of the T2K experiment is that it is an off-axis experiment, with the beam directed downward by about $2.5°$ with respect to the direction of SK. The reason is the following: in this configuration the neutrino energy spectra is more peaked and is less affected by the energy spread of the initial pion beam. In order to better understand this statement, the following example is proposed.

A pion with energy E_π decaying into a muon and the corresponding neutrino is consid-

ered. In the center of mass frame of the pion the two decay products are emitted back to back with the same momentum equal to p_0 and an angle φ with respect to the boost direction of the pion. Thus, the momentum of the neutrino can be decomposed into two components: the x-axis along the boost and y-axis parallel to the boost

$$\begin{aligned} p_\nu^{\mathrm{CM}} &= (p_0 \cos\varphi, p_0 \sin\varphi) \\ E_\nu^{\mathrm{CM}} &\approx p_0 \end{aligned}$$

where the neutrino was assumed massless. The neutrino energy in the laboratory frame can be obtained with a relativistic boost

$$\begin{aligned} E_\nu &= \gamma_\pi \left(E_\nu^{\mathrm{CM}} + \beta_\pi p_{\nu,x}^{\mathrm{CM}} \right) \\ &= p_0 \gamma_\pi \left(1 + \beta_\pi \cos\varphi \right) \\ p_\nu &= \left(p_0 \gamma_\pi \left(\beta_\pi + \cos\varphi \right), p_0 \sin\varphi \right) \end{aligned}$$

By using the expression for the momentum of the neutrino the angle θ in the laboratory frame can be obtained

$$\begin{aligned} \mathrm{tg}\theta &= \frac{p_{\nu,y}}{p_{\nu,x}} \\ &= \frac{1}{\gamma_\pi} \frac{\sin\varphi}{\beta_\pi + \cos\varphi} \end{aligned}$$

Using in the pion ultra-relativistic regime were $\beta_\pi \approx 1$[†]

$$1 + \gamma_\pi^2 \mathrm{tg}^2\theta \approx \frac{2}{1 + \cos\varphi}$$

So, by combining this expression and the one for the energy of the neutrino

$$E_\nu \propto \frac{E_\pi}{1 + \gamma_\pi^2 \mathrm{tg}^2\theta} = \frac{E_\pi}{1 + \left(\frac{E_\pi}{m_\pi} \right)^2 \mathrm{tg}^2\theta}$$

[†]This is not actually the case of the T2K experiment. Nonetheless such an approximation helps understand the qualitative behaviour.

At $\theta = 0$ the neutrino energy is directly proportional to the energy of the initial pion, thus the great pion energy spread will result in a spread in the neutrino beam energy. If, though, the angle is non-zero, the term depending on the angle modifies the energy behaviour: for a small pion energy linearity is preserved, while at high pion energies a decreasing E_π^{-1} trend is present. Thus there will be a certain pion energy leading to the maximum neutrino energy, with higher pion energy leading to neutrino energies lower than such a maximum value. This effect can be tuned in order to strongly limit the high energy behaviour of the neutrino spectra, peaking it to the value of interest with a proper choice of the angle.

2.3 The INGRID and ND280 near detectors

The T2K experiment pairs to SK two near detectors located at $280\ \mathrm{m}$ from the beam production site: INGRID (INteractive Netrino GRID) and ND280. The former is centered on the beam axis and allows a daily measurement of the neutrino beam profile. It consists of several identical modules placed in a cross shape, each one containing layers of iron plates and tracking scintillator planes read through WLS (WaveLength Shifting) fibers and MPPC (Multi-Pixel Photon Counter) detectors.

ND280, instead, is located off-axis in the direction of SK. This detector is magnetized using the magnet obtained from the UA1 experiment after being properly modified in order to comply with the Japanese anti-seismic regulations. In this way the detector is placed in a $0.2\ \mathrm{T}$ magnetic field allowing the determination of sign and momenta of the particles produced in neutrino interactions.

At the moment, the configuration of the ND280 subdetectors (figure 2.1) starting from upstream is the following. First there is the PØD, a scintillator tracking detector equipped with fillable water bags. Comparing the detection rate between when such bags are full or empty, it is possible to measure the interaction cross section in water. The specific interaction that needs to be studied is the production of a π^0 after the NC interaction of a neutrino with a nucleus

$$\nu + N \to \nu + N' + \pi^0 + X$$

Such interaction is an important background in SK: neutral pions, in fact, decay mainly into two energetic photons. The electromagnetic cascade they produce risks to be misidentified as an electron production event, thus producing an important background that needs to be well under control.

Then three TPCs are present: each one allows to track the particles produced by the interactions of ν with the FGDs (Fine Grained Detectors), measuring the emission angle, momentum, charge and type. The FGDs provide a target mass for the neutrino interactions inside of ND280. They are composed of several alternating planes of brass or water and of scintillator bars. These detectors allow the tracking of the particles that are produced with not enough energy to enter the TPCs.

TPCs, FGDs and PØD are then covered by a layer of electromagnetic sampling calorimeters (ECal), allowing an hermetic coverage of the particles emitted in the inner detectors. Moreover, the stopping of particles allows to measure their full energy, that gives additional informations useful for the particle's identification.

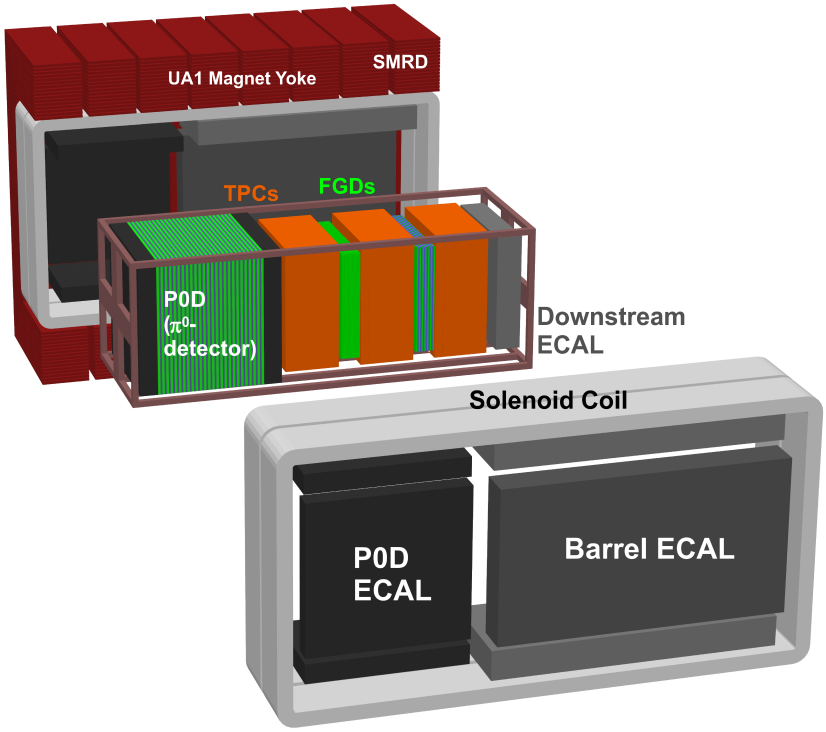

Figure 2.1: Schematical drawing of the ND280 detector.

2.4 ND280 upgrade

The use of TPCs allows a complete characterization of the leptons emitted in a neutrino interaction, which allows the determination of the flavour of such neutrino. This capability

is thus one of the key characteristic of the ND280 detector.

As a consequence of the positioning of such TPCs, the lepton detection efficiency is high in the forward region, but decreases abruptly for angle above about $50°$ with respect to the beam direction, as it is clear from figure 2.2. This effect is due to the fact that the great majority of the detector's target mass is located in the FGDs, thus, particles emitted at high angles do not traverse the TPCs and their identification is more complicated. Otherwise, it is noteworthy that the SK far detector, due to its structure, has a nearly 4π coverage.

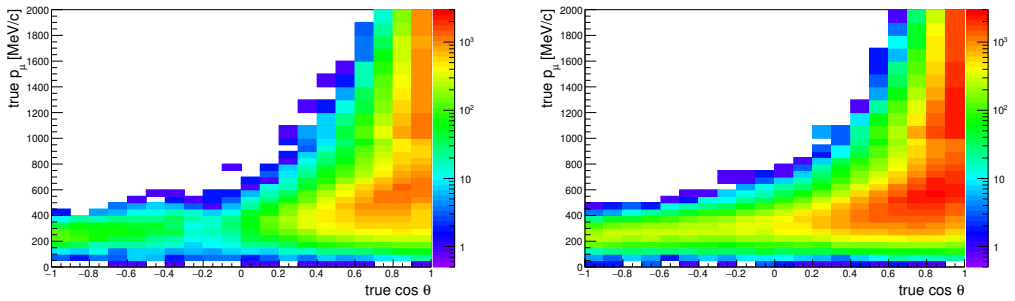

Figure 2.2: Comparison between the selected ν_μ event distribution between the current (left) and upgraded (right) version of ND280. A region with reduced efficiency is clearly visible for angles around $90°$. Figure taken from [8].

The collaboration started studies looking for ways to improve the near detector efficiency for high angle and low momentum particles. The upgrade modifies only the upstream part, with the removal of PØD and its substitution with a sandwich of two HA-TPCs (High Angle TPCs) and SuperFGD, a high granularity scintillation detector. In this way, an efficient reconstruction of particles emitted at high angles is possible, as shown in figure 2.2. Moreover, the detection of low energy electrons emitted inside of SuperFGD will allow the reduction of systematic uncertainties linked to the beam contamination of electron neutrinos.

The goal of this work of thesis is the comprehension of the HA-TPCs, particularly the resistive MICROMEGAS detector and the preparation of the prototype for testbeam experiments.

2.5 The HA-TPC

A drawing of the HA-TPC is shown in figure 2.3. The TPC volume is $2.0 \times 0.8 \times 1.8$ m^3, with the drift volume divided in half by the cathode positioned at the center. The readout anode is located on each side of the box, thus giving drift length of 90 cm. The volume is filled with the T2K gas mixture, composed of $Ar - CF_4 - iCH_4$ with a ratio respectively

of $95 - 3 - 2\%$, and will be kept at a pressure of 5 mbar above the atmospheric one. Each charge collection plane will be read with eight resistive MICROMEGAS, each having a pad size of 10×11 mm^2, for a total of 36864 pads.

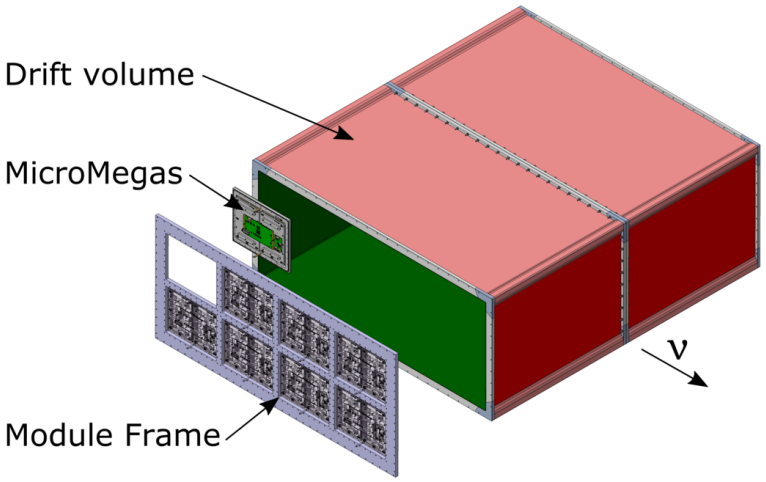

Figure 2.3: Schematic drawing of one of the two HA-TPCs for the upgrade of the ND280 experiment. Image obtained from [8].

In order to provide the uniform 275 V/m drift field, a voltage of 27 kV needs to be applied to the cathode. Such a high voltage is degraded with a voltage divider, each node of which is connected to strips forming the so-called field cage.

3

Particle detectors

3.1 Charged particle interaction with matter

A fast charged particle traversing a material interacts with its atoms in a variety of ways. For the comprehension of this work, though, only ionization and multiple scattering are important. In this section a brief introduction to the physics of these mechanisms is reported[2].

Ionization is the process where an energetic charged particle removes electrons from the atoms of a material. Such a process depends on the characteristics of the material, and on the energy and mass of the particle.

For a particle with speed β relative to the speed of light and $\gamma \equiv 1/\sqrt{1-\beta^2}$ such that $0.1 \lesssim \beta\gamma \lesssim 1000$, the mean energy loss per unit length is parametrized with the Bethe-Bloch formula

$$\langle -\frac{dE}{dx} \rangle = (4\pi N_A r_e^2 m_e c^2) z^2 \frac{Z}{A} \frac{1}{\beta^2} \left[\frac{1}{2} \log \frac{2 m_e c^2 \beta^2 \gamma^2 W_{\max}}{I^2} - \beta^2 - \frac{\delta(\beta\gamma)}{2} \right]$$

where N_A is the Avogadro constant, r_e is the classical electron radius, m_e is the electron's mass, c the speed of light, z is the charge of the particle, Z and A the atomic and mass number of the material, $W_{\max}$ is the maximum energy transfer to an electron in a collision, I is the mean excitation energy for the material while δ is a correction coefficient. Here length is considered as the actual geometrical length times the density of the material.

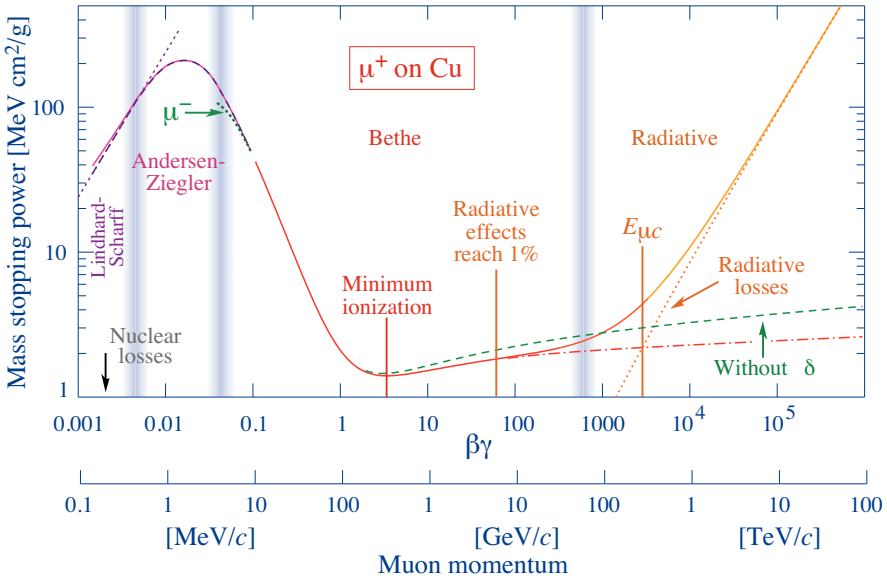

Figure 3.1: Graph showing the energy loss of a muon in copper as a function of its momentum. Image taken from [2].

Such a formula has a well known behaviour. As shown in figure 3.1 above $\beta \approx 0.1$ it is decreasing, reaching a minimum for a $\beta\gamma$ between about 3 and 3.5. It then slowly increases until the so called radiative losses come into play. This effect consists in the emission of high energy photons due to the strong acceleration produced by the interaction with the field of the nuclei. It is important to notice that, due to their lower mass, this represents the main interaction mechanism for high energy electrons.

Another important effect affecting particle detectors is the production of δ rays. In this phenomena, one of the ionized electrons obtains sufficient energy to travel a sizeable distance in the material while producing additional ionization. A picture of such an event is reported in figure 3.2.

An additional effect involves the great number of small deflections mainly due to the interaction with the Coulomb nuclear field of the material. For particles with velocity close to the speed of light, the deflection angle is inversely proportional to the particle's momentum and goes as the square root of the material's thickness. Such an effect is important to take into account specifically in tracking detectors where this kind of deflections negatively impact the obtainable resolution.

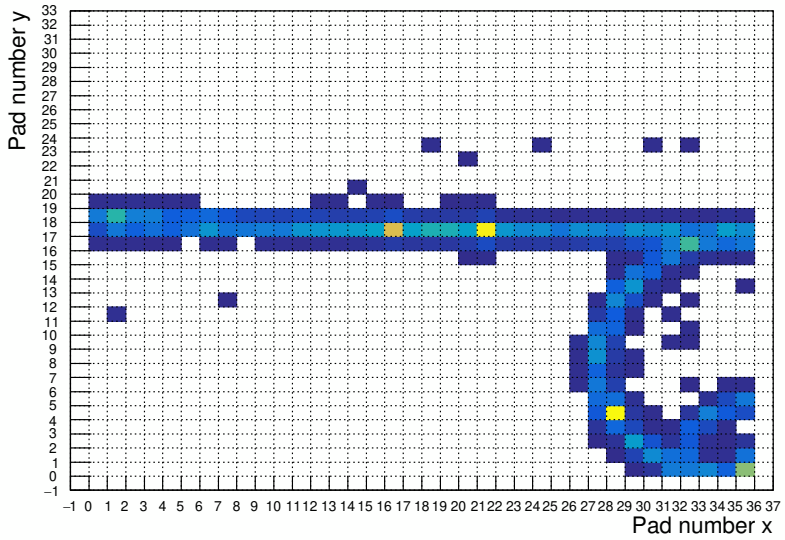

Figure 3.2: Example of a delta ray event in the prototype of the HA-TPC that will be described in the later chapters. A $4\ \mathrm{GeV}/c$ electron (horizontal track) scatters on the the electrons of the gas (circular track), transfering a momentum in the order of $5\ \mathrm{MeV}$.

3.2 Gaseous detectors

A particle detector is a device that allows to convert the energy released by a particle inside of its active volume into an electrical signal. If this active material is a gas then it is called a gaseous detector[9].

The electron and ion pairs left after the passage of a charged particle will drift if an electric field is applied. The drift velocity is usually expressed as

$$v = \frac{e}{m} E \tau$$

where e and m are respectively the electron's charge and mass, E is the modulus of the electric field and τ is the average time between collisions with the gas molecules. Due to the high number of such collisions the drift velocity appears constant. Moreover, an effect of both lateral and longitudinal diffusion can be observed. In the case where a magnetic field is present the situation is different, as the Lorentz force on the electrons is relevant. The drift velocity

of electron in this situation obeys the Langevin equation

$$m\frac{d\vec{v}}{dt} = -\frac{e}{\mu}\vec{v} - e(\vec{E} + \vec{v} \times \vec{B}) + \vec{\eta}(t)$$

where μ is the mobility. In this equation the three terms in the right hand side represent different effects: the first is viscous friction, which allows to reach a constant limiting speed given by the field, the second one is the electromagnetic force due to the external electric and magnetic fields, while the last one is a stochastic term giving rise to Brownian motion. The solution to this equation is the following

$$\vec{v} = -\frac{\mu}{1+\omega^2\tau^2}\left(\vec{E} + \frac{\vec{E}\times\vec{B}}{B}\omega\tau + \frac{\vec{E}\cdot\vec{B}}{B^2}\vec{B}\omega^2\tau^2\right)$$

where $\omega = eB/m$.

This formula has a peculiar behaviour. When the magnetic field is parallel to the electric field, the drift velocity is modified. When they are perpendicular, on the other hand, electrons will drift at an angle called the Lorentz angle. Additionally, the presence of a magnetic field has a strong impact on diffusion: if it is parallel to the electric field, the spiraling of the drifting electron around the magnetic field line greatly reduces the transverse diffusion, thus improving the resolution of the detector.

Moreover, for a strong enough electric field, electrons can be accelerated to a velocity sufficient to further ionize the gas. This process is known as avalanche amplification.

Depending on the electric field, different amplification regimes exist as shown in figure 3.3. After the secondary ionization process is initiated, the gas is in the so-called proportionality regime, characterized by a charge production proportional to the initial charge. At an even greater field, the limited proportionality regime is reached. Here a saturation effect starts to take place, reducing the amount of charge produced. At even higher fields, in the Geiger-Mueller regime, no proportionality is present: ionization events produce a discharge of the same magnitude. In such a case a mean to stop the avalanche discharge is needed, for example the electric field is reduced or a special quenching gas is added to the gas mixture.

Together, drift and amplification processes can be used to collect and amplify the charge. At this point it is possible to produce an electrical signal. To do this a grounded electrode is added, an induced charge will form on it. The drift of electrons and ions will cause this induced charge to vary in time, thus creating a current from/to ground that can be read with

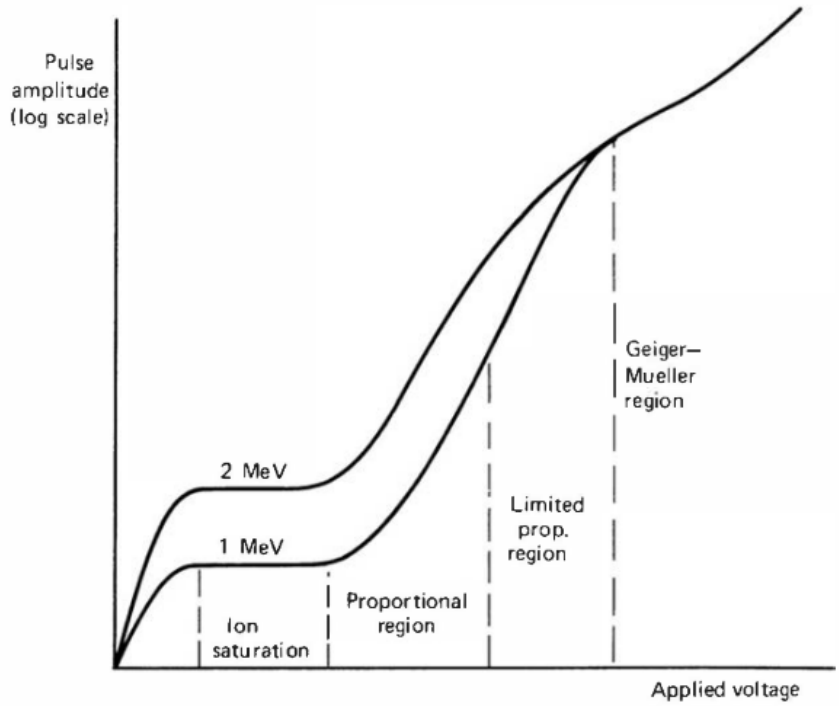

Figure 3.3: Signal output for two different energy deposit as a function of the applied voltage for a gas detector. Picture taken from [10].

the proper electronic signal chain.

These are the basic building block of a gaseous detector, the signal formation will be more thoroughly discussed in section 5.5 on page 34 of this work.

3.3 The Time Projection Chamber

A TPC (Time Projection Chamber) is a particular type of gas detector. In the active region a uniform electric field is applied in order to transport the charge, produced in a ionization event, to a plane where it is amplified and collected. Electrons are usually the charge carriers of choice because they drift much faster than ions and thus allow a fast detector response.

The charge collection plane is usually segmented in order to obtain a 2D reconstruction of the event. Furthermore, thanks to the uniform electric field the charge drifts at a constant speed so by measuring also its time of arrival a full 3D reconstruction of the event can take place.

The addition of a magnetic field allows the measurement of the traversing particle's mo-

menta, although its addition must be designed with care. In fact, the electrons and ions movement is also affected by the magnetic field. A common configuration, that will also be used in the following sections, is the one where electric and magnetic field are parallel to each other. This in turn modifies the drift velocity and charge transverse spread.

3.4 MICROMEGAS

In the previous section the main idea behind TPCs was discussed. This section will instead explain how the amplification of the electrons produced by ionization is carried out once they arrive to the collection plane. The amplification device of interest for this work are the MICROMEGAS (MICRO MEsh GAseous Structures).

Such a device consists of a mesh separating a small gaseous gap of thickness $\approx 100\ \mu m$ from the active TPC volume (figure 3.4) and a collection plane segmented into metallic pads or strips. Between the mesh and the pad plane there is a voltage difference such that an intense electric field is produced in the gap. When an electron from the active volume enters such a region it is accelerated and produces an avalanche, thus amplifying the signal. Compared to other amplification devices such as Gas Electron Multipliers (GEMs) its main advantage is that the ions from the avalanche are neutralized by the mesh, thus maintaining a clean TPC active volume with reduced space-charge effects.

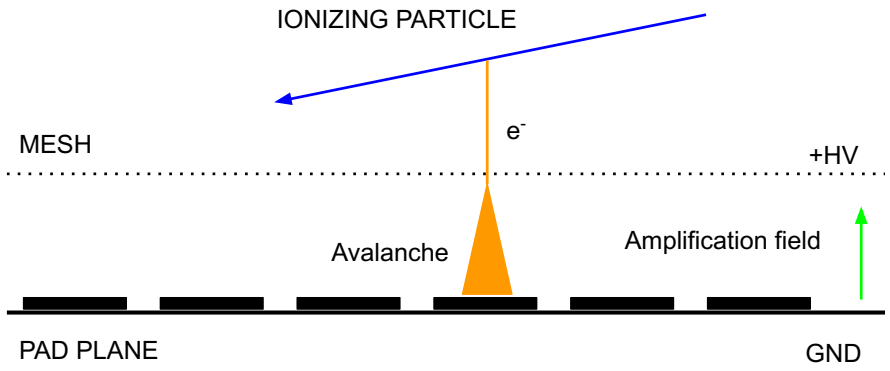

Figure 3.4: Schematic representation of a conventional MICROMEGAS with the avalanche produced by an electron created by an ionizing track.

The electron and ion pair produced in the avalanche then drift, thus producing an electric signal on the pads. It is important to notice that usually the electron signal is fast, thus the slower ion signal is used.

One of the issues that such a design poses is that an high voltage terminal (the mesh) needs to be placed into close proximity to the pads at which the front-end electronics is connected. Without proper protection circuitry a spark can cause the failure of one or more acquisition channels. Depending on the experiment this might be either costly, difficult to repair, or both. On the other hand, the addition of such protection circuitry might take up additional space (see figure 3.5), that can be problematic because it can create dead layers or occupy space in a magnetic field.

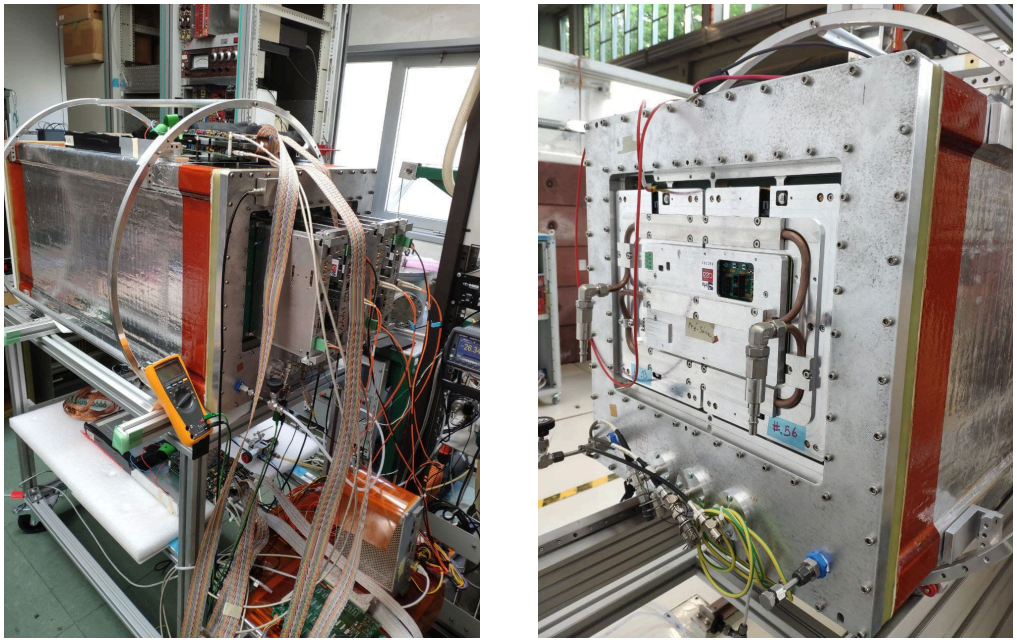

Figure 3.5: Picture comparing the old electronics (left) with spark protection with the new one without it (right).

A solution allowing the protection of the electronics and reducing the space occupied is to include a resistive layer in the gap between the pad and the mesh. Such a layer can be glued to the pad with an insulating material. The conductivity of such a component is critical: if it is too high it will behave like a perfect conductor, effectively shielding the pad underneath and thus making it impossible to extract a signal; if it is too low, on the other hand, a spark will not discharge itself through it and thus still damage the electronics. If the right value is chosen this layer will behave in such a way as to be transparent to the induction signal of electrons and ions, while still protecting the electronics connected to the pads.

Moreover an additional interesting effect takes place: electrons produced in the gap now reach the resistive layer. Once there they will diffuse to its edge. Such a movement will also

induce a signal on the pads underneath. This effects will be examined in greater detail in the dedicated section 5.4 on page 33.

4

The HA-TPC prototype

In order to thoroughly test the technology needed to build the High Angle TPCs of the T2K experiment two prototypes were built. In this work the preparation and first tests of the second prototype will be described.

4.1 Field cage

A TPC needs a constant and uniform electric field in its active volume to avoid distortions during the drift of the electrons. Such a field is produced by applying an high negative voltage on the cathode, while keeping the anode grounded. This, though, is not sufficient to get the desired field uniformity. A series of metallic rings enclosing the active volume are added, each with the voltage linearly decreasing from anode and cathode. This decreasing voltage pattern is produced thanks to a resistive voltage divider.

The design of such a field cage is not trivial: it needs to be gas tight in order to keep a controlled gas mixture with contamination of water and oxygen at the part per million level. Moreover the degradation of the high voltage to the external conductors is needed. An additional constraint is defined by the multiple scattering phenomena: if the field cage is too thick, the additional scattering negatively impacts the momentum determination.

The technology tested is based on strips deposited on a Kapton foil that is then glued to the mechanical structure of the field cage. This structure is made of a composite material consisting of polyamide sheets, fiber-fabrics peels and honeycomb panels as spacers. In this

structure, G10 flanges are embedded in order to allow a tight seal on the endcaps. Each strip of the field cage is 3 mm wide with a pitch of 5 mm, the ones on the side facing the active volume are called "field strips", while the ones staggered on the opposite side are called "mirror strips". These strips are accessed through pads with viases penetrating the insulating foil. A drawing of the geometry of the field cage is shown in figure 4.1. The two voltage dividers (for redundancy) are built using 5 MΩ SMD resistors. The overall resistance from anode to cathode is 1 GΩ.

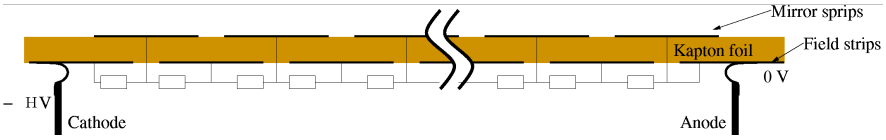

Figure 4.1: Schematic drawing showing a cross section of the field cage, with the staggered mirror and field strips, together with the voltage divider's resistors and the connection to cathode and anode.

Several operations were needed before high voltage could be applied to the detector. First the continuity of the field strips was tested. This showed that some of them were interrupted and they had to be repaired. Later, the continuity of the mirror strips was verified by measuring the capacitance with one of the nearby field strips. If it was interrupted, a reduction in capacitance would be observed due to the reduced overlap length. This test showed that all the mirror strips were in good condition.

Moreover a test verifying the presence of shorts between different strips was performed, indicating a short between a mirror and a field strip in the region were the foil was cut. This was due to a carbon fiber that was deposited during the production. The defect was removed with a file.

At this point the strip quality was verified and it was time to solder the eight hundred resistors of the voltage divider. After this, the value of each resistor was verified by applying a proper voltage. Such an operation allows to test that the viases are properly connected to the mirror strips. A few were found to be not working and needed a repair.

After these last repairs, the cathode and a test anode were connected and the first high voltage tests were performed in air up to 35 kV. No leakage current that might be due to unwanted ohmic paths to ground, possibly leading to discharges, was observed. Later this test was repeated with pure argon, having a lower dielectric breakdown voltage.

4.2 Gas system

In order to allow the operation of the detector within the required specifications, a low degree of contamination of water and oxygen (both below 50 ppm) is needed. This is important because water affects the interaction of electron leading to a reduction of the drift velocity while oxygen leads to electron attachment, in this way reducing the amount of charge reaching the collection plane. In addition to provide the active medium, the gas needs to be continuosly fluxed in order to remove contaminants desorbed from the inner surface of the chamber. The gas system is providing gas that is not recirculated, with a flow $30\ \mathrm{L/h}$ which in turn keeps the chamber's pressure a few tens mbar above the atmospheric one.

4.3 DAQ

The resistive MICROMEGAS detector (ERAM-01) is connected to four ARC (Another Readout Card) electronics cards. Four AFTER (ASIC For TPC Electronic Readout)[11] front-end chips, sampling 72 pad signals, are present on each card, together with an ADC (Analog to Digital Converter) and a FPGA (Field Programmable Gate Array) chip taking care of the communication with the back-end electronics.

Each channel of the AFTER chip has the following electronic chain (figure 4.2). First the signal is amplified and integrated with charge sensitive amplifier with variable gain from 120 to $600\ \mathrm{fC}$. The signal is then fed into a pole-zero cancelling stage to avoid undershots in the output signal. At this point the signal is shaped with a RC^2 Sallen-Key filter followed by an amplification stage with gain -2. The shaped and amplified signal is stored into an analog memory based on a circular buffer of 511 capacitors per channel, called an SCA (Switched Capacitor Array).

In this way it is possible to perform a continuous analog sampling of the signal. When the trigger signal arrives, the writing of the SCA is stopped and each capacitor voltage is multiplexed to the ADC in the ARC card. In this way it is possible to sample several hundreds of channels with just a single ADC, although with the trade-off of an higher dead time.

The back-end electronics is based around a TDCM (Trigger and Data Concentration Module) that is connected to the ARC cards and takes care of the synchronization and the trigger distribution. Moreover, this module performs zero-suppression, baseline equalization of the channels and merges the data frames coming from the front-end building complete events.

The TDCM is connected to a computer taking care of the configuration of the electronics, the storage of the events, slow control and monitoring.

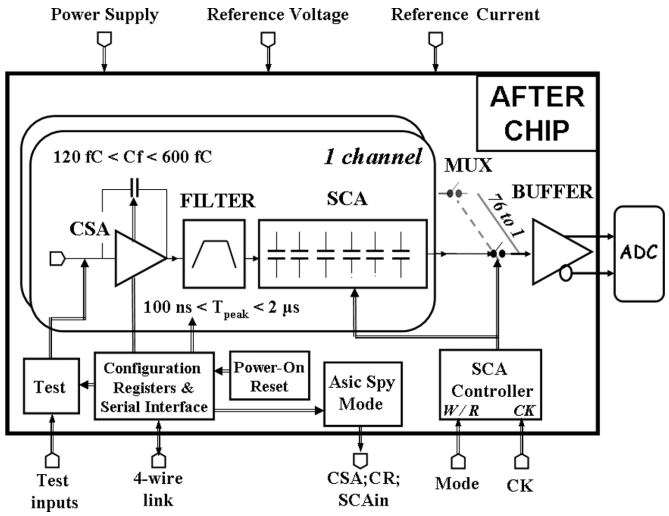

Figure 4.2: Block diagram of the AFTER chip: the front end CSA and filter and SCA are shown. Picture from reference [11].

4.4 First data acquisition

After the installation of the DAQ and when the gas purity inside of the TPC attained a sufficient level it was possible to acquire data. A square plastic scintillator with a surface of 15×15 cm^2 read by a PMT was used as a trigger. By looking at tracks crossing cathode and the anode it was possible to estimate the drift velocity of electrons which agreed with expectations (7.8 cm/µs at 275 V/cm drift field).

4.5 DESY test beam

The prototype was then transported to Hamburg at the Deutsches Elektronen-Synchrotron (DESY)[12] in order to perform a full characterization of the detector, including the new version of the electronics. Here it was possible to employ the T24 experimental area, where a superconducting magnet enabled the test of the TPC in a magnetic field up to 1 T. The magnet is located on a movable platform which allows translations and rotation. A beam of 4 GeV electrons with an intensity ranging from a few Hz to 2 kHz was used for scanning the detector. Specifically, scan along the drift direction allow the characterization of drift

velocity and transverse diffusion. Data at two drift fields were taken, namely $275\ \mathrm{V/cm}$ were the velocity reaches a plateau at the maximum value, and at $140\ \mathrm{V/cm}$ where the diffusion is minimal. Moreover, several vertical and angular scans were performed in order to study the non-uniformities of the TPC field. In addition, such a scan provides data that will be used to measure the charge spread time constant of the ERAM detector. This topic will be covered in detail in a later chapter. Angular scans, instead, allow to study the reconstruction of inclined tracks.

A picture of the TPC inside of the superconducting magnet is shown in figure 4.3.

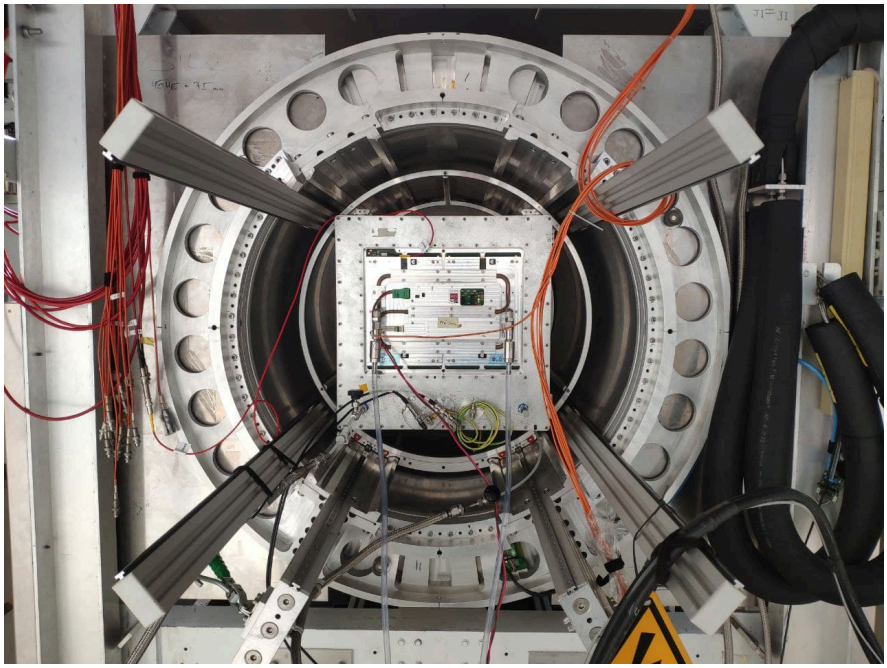

Figure 4.3: Picture of the HA-TPC prototype inside of the magnet at DESY.

5

Signal formation in ERAM detectors

The ERAM (Encapsulated Resistive Anode MICROMEGAS) detector is the resistive MICROMEGAS used for the HA-TPCs of the ND280 upgrade. They consist of a PCB (Printed Circuit Board) were 1152 pads, each with dimension of $10.09 \times 11.18\ \mathrm{mm}^2$ are spread over a surface of $32 \times 36\ \mathrm{cm}^2$. Each pad is then routed through the board to the connectors for the electronics cards. On top of the pads an insulation layer is placed, composed of $150\ \mu\mathrm{m}$ of glue and $50\ \mu\mathrm{m}$ of APICAL foil, on top of which a layer of DLC (Diamond Like Carbon) was deposited through sputtering. This latter layer is the resistive one, with a surface resistivity of around $0.3\ \mathrm{M}\Omega/\square$. On top of this is positioned the mesh, after an amplification gap of $128\ \mu\mathrm{m}$.

In order to better understand the behaviour of such a detector, an introduction to the physics of the charge on resistive layers will follow, alongside the experimental studies carried out to try characterizing them.

5.1 Surface resistivity

The second Ohm's law allows to obtain the resistance R of a conductive wire given its length l, its cross sectional surface S and the material dependent parameter know as resistivity ρ, measured in Ω/m

$$R = \frac{\rho l}{S}$$

If this law is combined with the first Ohm's law, stating that for an ohmic conductor the resistance is the proportionality constant between current and voltage, a vectorial expression can be obtained

$$\vec{E} = \rho \vec{j}$$

where $\vec{E}$ is the electric field inside of the material and $\vec{j}$ is the current density linked to such a field. An important quantity linked to the resistivity is its reciprocal, the conductivity, denoted by $\sigma = \rho^{-1}$.

When the conduction inside of a thin sheet of thickness a is considered, the surface of the conductor can be written as the product of such thickness and of the width w of the sheet. Thus the second Ohm's law can be rewritten as

$$R = \frac{\rho}{a}\frac{l}{w} \equiv R_S \frac{l}{w}$$

where R_S is the sheet resistance. Such a value is dimensionally a resistance, but in order to distinguish it from a normal resistance it is measured in $\Omega/\square$.

The vectorial form of Ohm's law can be updated as

$$\vec{E}_{2\mathrm{D}} = R_S \, \vec{j}_{2\mathrm{D}}$$

here $\vec{E}_{2\mathrm{D}}$ is the electric field in the plane of the sheet, while $\vec{j}_{2\mathrm{D}}$ is the two-dimensional current density, measured in $\mathrm{A/m}$. Such an expression is equivalent to integrate the previous vectorial equation along the thickness of the sheet.

5.2 Electromagnetism with conductors

The laws governing the electromagnetism are the Maxwell's equation, reported below in the SI unit form

$$\begin{cases} \nabla \cdot \vec{D} = \rho_f \\ \nabla \cdot \vec{B} = 0 \\ \nabla \times \vec{E} = -\frac{\partial \vec{B}}{\partial t} \\ \nabla \times \vec{H} = \vec{j}_f + \sigma \vec{E} + \frac{\partial \vec{D}}{\partial t} \end{cases}$$

where ρ_f and $\vec{j}_f$ are the externally impressed charge and current densities, $\vec{D} = \epsilon \vec{E}$ and $\vec{H} =$

$\vec{B}/\mu$ are respectively the displacement and magnetizing field in the case of linear materials. Notice how in the last equation an additional term was added in order to take into account the flow of current due to the resistivity of the material.

If the divergence of the last equation is computed, the continuity equation governing charge conservation is obtained

$$\nabla \cdot \left(\nabla \times \vec{H} \right) = 0$$
$$\frac{\partial \rho_f}{\partial t} + \nabla \cdot \left(\vec{j}_f + \sigma \vec{E} \right) = 0$$

In the case of slowly varying charges an useful regime is the quasi-electrostatic approximation, where

$$\frac{\partial \vec{B}}{\partial t} \approx 0 \implies \nabla \times \vec{E} \approx 0$$

This allows in turn to express the electric field as the gradient of a potential φ, namely $\vec{E} = -\nabla \varphi$.

5.3 Free charges in ohmic conductors

Considering a given charge density inside of an infinite ohmic conductor with uniform conductivity σ and electric permittivity ϵ, the continuity equation, in absence of external currents, can be written as

$$\frac{\partial \rho_f}{\partial t} = -\sigma \nabla \cdot \vec{E} = -\frac{\sigma}{\epsilon} \nabla \cdot \vec{D} = -\frac{\sigma}{\epsilon} \rho_f$$

where the uniformity is an important requirement, necessary to add the ϵ factor inside of the divergence. In this way, thanks to the first Maxwell equation, an expression involving only the charge density is obtained.

Such an expression is also easily solvable giving

$$\rho(\vec{x}, t) = \rho(\vec{x}, 0) e^{-\frac{t}{\tau}}$$

with $\tau = \epsilon/\sigma$. The charge distribution undergoes a process known as charge relaxation were it simply decays to zero. This result might seem shocking: for a point charge Q in a given point in space, the result is simply that charge decaying with a characteristic time τ. At first, it might seem like charge is not conserved, as this is indeed the case.

A more enlightening situation is the one of a charge Q located at the center of a uniform conducting sphere of radius R in free space. The same calculation performed above applies everywhere except on the surface of the sphere. There, if a cylinder C of infinitesimal surface A and height h is taken, the continuity equation in the general case can be integrated

$$\frac{\partial}{\partial t}\int_C \rho dV + \int_C \nabla\cdot\left(\sigma\vec{E}\right)dV = 0$$

The application of Gauss's theorem on the second integral, transforming it into an integral on the surface of the cylinder, gives

$$\frac{\partial q}{\partial t} + \int_{\text{top of } C}\sigma\vec{E}\cdot d\vec{A} + \int_{\text{bottom of } C}\sigma\vec{E}\cdot d\vec{A} + \int_{\text{side of } C}\sigma\vec{E}\cdot d\vec{A} = 0$$

where q is the charge inside of the cylinder. Notice that in free space the conductivity is zero, thus the first term vanishes. Moreover also the term corresponding to the side of C vanishes, due to its vanishing height and for symmetry reasons. So

$$\frac{\partial q}{\partial t} = -\int_{\text{bottom of } C}\sigma\vec{E}\cdot d\vec{A} = A\sigma E$$

where the orientation of the cylinder surface gives the minus sign in the last equality. At this point, substituting the electric field for a charge at the center of a dielectric sphere, one obtains

$$\frac{\partial q}{\partial t} = Q(t)\frac{\sigma}{\epsilon}\frac{1}{4\pi R}$$

where q here is the surface charge density. Integrating over the surface of the sphere, i.e. multiplying by $4\pi R$, one obtains an expression for the charge that moved to the surface

$$\frac{\partial Q_{\text{surface}}}{\partial t} = Q(t)\frac{\sigma}{\epsilon} = Q\frac{1}{\tau}e^{-\frac{t}{\tau}}$$

if the above is integrated over time from $t = 0$ to a given time t, the resulting value is

$$Q_{\text{surface}}(t) = Q\left(1 - e^{-\frac{t}{\tau}}\right)$$

Notice how in this case charge is clearly conserved, in fact $Q_{\text{surface}}(t) + Q(t) = Q$ at all times. The issue with the previous model is that, without a boundary, the charge migrated to infinity and got lost. Another important remark is the following: in this simplified case

the only charge producing an electric field in the conductive region is the one at the center. In general, though, this is not true. The charge at the surface will in turn produce an electric field that will influence the current density.

5.4 Free charge on a conductive sheet

Another interesting case is the one of a charge on a resistive sheet with surface conductivity R_S. This case, even though apparently simple, is difficult to solve. A solution in the limiting case of an infinite thickness parallel plate capacitor is reported in reference [13].

If a charge Q is positioned at the origin at time $t = 0$, the surface charge density is

$$q(r,t) = \frac{Q}{2\pi} \frac{vt}{(r^2 + (vt)^2)^{3/2}}$$

where $v = (2\epsilon R_S)^{-1}$. This solution corresponds to the charge distribution induced on an ideal conductor plane, with the charge moving with velocity v in the direction orthogonal to it.

Such a solution is difficult to obtain from simple electrostatic consideration. In fact, if one tries to compute the potential produced by a rotationally symmetric distribution $q(r)$ the following integral appears

$$\varphi(r) = \int_0^{+\infty} \eta \, d\eta \int_0^{2\pi} d\theta \, \frac{q(\eta)}{4\pi\epsilon} \frac{1}{\sqrt{(r - \eta\cos\theta)^2 + (\eta \sin\theta)^2}}$$

this complicated elliptic integral then needs to be substituted inside of the continuity equation, this time in the bidimensional case

$$\frac{\partial q}{\partial t} = -\frac{1}{R_S} \nabla_{2\mathrm{D}} \cdot \vec{E} = \frac{1}{R_S} \nabla^2_{2\mathrm{D}} \, \varphi$$

here the 3D continuity equation was integrated along the z axis, thus producing a surface density on the left hand side and a bidimensional divergence on the right hand side.

This last formula is indeed satisfied by the solution above, but obtaining such an expression from the above equations is not at all trivial.

A related situation, geometrically similar to an ERAM detector, corresponds to the addition of a ideally conducting grounded plane parallel to the previous one at a distance d. In reference [13] a complete analytic solution of this problem is reported. If the above situation

is seen as a parallel plane capacitor an useful approximation can be obtained. In such a case, the potential φ at a given point will be proportional to the charge q on such a point, that will induce another charge on the ideal plane of value $-q$. This situation clearly resembles a parallel plane capacitor, so it is possible to write

$$Q = C\,\Delta V \qquad\qquad q = C\,\varphi$$

The formula on the left is the well known one defining the capacity C in terms of the charge Q on a capacitor where a potential difference ΔV is applied. This formula is valid for the complete capacitor. On the left side, instead, a local formula is written, linking the charge **density** at a given location to its potential. This is equivalent to dividing the system above into a great number of infinitesimal capacitors. In this case, C represents the capacity per unit area. If such an equality is substituted inside of the continuity equation, it results in

$$\frac{\partial q}{\partial t} = \frac{1}{R_S C}\nabla^2_{\text{2D}}\, q$$

This equation is called the 2D Telegrapher's equation[14], as it resembles a 2D version of the completely lossy equations used to study transmission lines. Remarkably, this equation is also the 2D diffusion equation, with a diffusivity given by the $R_S C$ constant.

Despite its simplicity and ease of use this expression needs care in order to be used in a simulation. First of all for time and distance scales much smaller than the diffusion's, the induced charge on the perfectly conductive plane is not exactly equal to the one above it, thus even for a point charge at time $t = 0$ this will appear to be already partially diffused. Moreover, the geometry of an ERAM is different: the conductive mesh behaves as an additional charge plane on the other side of the Ohmic sheet. This, will in turn induce charge on the lower one. Moreover, these induced charges will produce an electric field that influences the evolution of the charge spread.

5.5 Shockely-Ramo's theorem

A well known result of electrostatic applied to detectors is the Shockely-Ramo's theorem. This states that, if there is a charge q with velocity $\vec{v}$, it is possible to calculate the current induced on a grounded electrode, when all other metals are grounded, using the formula

$$I(t) = -q\vec{E}_W(\vec{x}) \cdot \vec{v}(t)$$

where $\vec{E}_W$ is the weighting field, defined as the field when the potential on the electrode is set to one, while all other conductors are grounded. This result is important, as it shows that the signal is produced not by the charge reaching the electrode, but rather by electrostatic induction.

Such a result is proven using the reciprocity theorem. This theorem states that, if there are i conductors enclosed into a region of space, for two configuration of voltages and charges (V_i, Q_i) and $(\bar{V}_i, \bar{Q}_i)$ it holds that

$$\sum_i Q_i \bar{V}_i = \sum_i \bar{Q}_i V_i$$

If two correct configurations are chosen, it is possible to prove Shockley-Ramo's theorem. It is important, though, to consider the charge q as a very small conductor with a deposited charge equal to q. This special conductor will be the zero-th of the following treatment:

- Detector configuration: $V_i = 0$ unknown Q_i for $i \neq 0$, while $Q_0 = q$
- Weighting field configuration: $\bar{V}_n = 1$ and $\bar{V}_i = 0$ unknown $\bar{Q}_i$ for $i \neq 0$, while $\bar{Q}_0 = 0$

It is important to notice that an infinitesimal conductor with no charge deposited will have the same potential as the point it is located in. If this was not the case a radial electric field would be produced by the potential difference, thus it will behave in the same manner as if it was charged, that is absurd. So, $\bar{V}_0$ will have the value of the weighting potential at the position of the charge, $\bar{V}_0 = V_W(\vec{x})$. Substituting these values inside of the reciprocity theorem gives

$$q\bar{V}_0 + Q_1 = 0 \implies Q_1 = -qV_W(\vec{x})$$

If this expression is derived over time, the current signal on the electrode is obtained by simple application of the chain rule

$$I(t) = \frac{dQ_1}{dt} = -q\frac{d}{dt}V_W(\vec{x}(t)) = -q\nabla V_W(\vec{x}) \cdot \frac{d\vec{x}}{dt} = q\vec{E}_W(\vec{x}) \cdot \vec{v}$$

For completeness, a proof of the reciprocity theorem is reported. Starting from Gauss's theorem

$$\iint_A \vec{K} \cdot d\vec{S} = \iiint_V \nabla \cdot \vec{K} dV$$

If two fields φ and ψ are taken, by building the auxiliary vector field $\vec{K} = \varphi\nabla\psi$ and $\vec{K}' = \psi\nabla\varphi$, their substitution into the above formula gives

$$\iint_A \varphi\nabla\psi \cdot d\vec{S} = \iiint_V \nabla\cdot(\varphi\nabla\psi)dV = \iiint_V (\varphi\nabla^2\psi + \nabla\varphi\cdot\nabla\psi)dV$$
$$\iint_A \psi\nabla\varphi \cdot d\vec{S} = \iiint_V \nabla\cdot(\psi\nabla\varphi)dV = \iiint_V (\psi\nabla^2\varphi + \nabla\psi\cdot\nabla\varphi)dV$$

If the two expression are subtracted this results in

$$\iint_A (\varphi\nabla\psi - \psi\nabla\varphi)\cdot d\vec{S} = \iiint_V (\varphi\nabla^2\psi - \psi\nabla^2\varphi)dV$$

Applying this formula in the reciprocity's theorem case, namely when φ and ψ are potentials, i.e. solution of the Laplace's equation in the volume V so $\nabla^2\varphi = \nabla^2\psi = 0$ it becomes

$$\iint_A (\varphi\nabla\psi)\cdot d\vec{S} = \iint_A (\psi\nabla\varphi)\cdot d\vec{S}$$

If the volume contains a number of conductors the surface integral on them will be peculiar: the field before the nabla will be constant, because it is evaluated on a conductor. Thus, it can be extracted for the integral and, using Gauss's theorem for the electric field:

$$\sum_i \varphi_i \iint_{A_i} (\nabla\psi)\cdot d\vec{S} = \sum_i V_i \iint_{A_i} (-\vec{E})\cdot d\vec{S} = \sum_i V_i \frac{\bar{Q}_i}{\epsilon}$$

Performing an identical calculation on the other side proves the theorem.

5.6 Finite Element Simulation

In order to understand the effects discussed at the end of the section 5.4 on page 33 and in order to study the impact of the drift of ions in the amplification gap on the Ohmic layer, a full finite elements electrostatic simulation was developed in C++. As discussed in the previous section, the charge induced on an electrode produces the signal, so this simulation allows not only to study the charge spread, but also the signal formation.

A box of size $l_x \times l_y \times l_z$ was discretized into $n_x \times n_y \times n_z$ cells, each with a step size in each direction of h_x, h_y and h_z. Using the quasistatic approximation where

$$\vec{E} = -\nabla\varphi$$

and substituting it in the first of Maxwell's equations, one obtains

$$\nabla \cdot \vec{D} = \nabla \cdot (\epsilon \vec{E}) = \rho_f$$

or

$$\epsilon \nabla^2 \varphi + (\nabla \epsilon) \cdot (\nabla \varphi) = -\rho_f$$

The above expressions needs now to be discretized. There are several ways in which this operation can be performed. Two of them where tested. The first one consists in the following:

$$\varphi(\vec{x}) \rightarrow \varphi(x, y, z)$$
$$\epsilon(\vec{x}) \rightarrow \epsilon(x, y, z)$$

where now x, y and z represent the index of the cell. At this point care needs to be taken in order to compute the derivatives with the greatest possible accuracy. A well known expression, stemming from the definition of derivative, is

$$\frac{df}{dx} \approx \frac{f(x+1) - f(x)}{h_x}$$

notice how in $f(x+1)$ the function is defined on cell index, thus equivalent to evaluating the undiscretized function in $f(x+h_x)$. Using a Taylor expansion, one notices the following

$$\frac{f(x+1) - f(x)}{h_x} = \frac{f(x) + f'(x)h_x + O(h_x^2) - f(x)}{h_x} = f'(x) + O(h_x)$$

A different expression can be used, leading to

$$\begin{aligned}
&\frac{f(x+1) - f(x-1)}{2h_x} = \\
=&\frac{f(x) + f'(x)h_x + \frac{1}{2}f''(x)h_x^2 - f(x) + f'(x)h_x - \frac{1}{2}f''(x)h_x^2 + O(h_x^3)}{2h_x} = \\
=&f'(x) + O(h_x^2)
\end{aligned}$$

here the cancellation of the second order terms allows the derivative to be computed with a much higher accuracy.

In a completely similar way the second derivative can be defined as

$$\frac{d^2 f}{dx^2} = \frac{f(x+1) - 2f(x) + f(x-1)}{h_x^2} + O(h_x^2)$$

By using these expressions the first of Maxwell's equations for a cell x, y and z becomes

$$\begin{aligned}
&\frac{1}{4h_x^2}\left(\epsilon(x+1) - \epsilon(x-1)\right)\left(\varphi(x+1) - \varphi(x-1)\right) + \frac{\epsilon}{h_x^2}\left(\varphi(x+1) + \varphi(x-1)\right) + \\
&+\frac{1}{4h_y^2}\left(\epsilon(y+1) - \epsilon(y-1)\right)\left(\varphi(y+1) - \varphi(y-1)\right) + \frac{\epsilon}{h_y^2}\left(\varphi(y+1) + \varphi(y-1)\right) + \\
&+\frac{1}{4h_z^2}\left(\epsilon(z+1) - \epsilon(z-1)\right)\left(\varphi(z+1) - \varphi(z-1)\right) + \frac{\epsilon}{h_z^2}\left(\varphi(z+1) + \varphi(z-1)\right) - \\
&-2\epsilon\left(\frac{1}{h_x^2} + \frac{1}{h_y^2} + \frac{1}{h_z^2}\right)\varphi = -\frac{Q}{h_x h_y h_z}
\end{aligned} \tag{5.1}$$

where, in order to have a cleaner expression, indexes equal to x, y and z were omitted. Moreover, the charge density was substituted with the amount of charge Q in the cell, divided by the cell's volume. Notice this formulation can be used in the case were the step size are different in each direction.

It is noteworthy, however, that in the above case the dielectric constant is defined in the same position as the potential. A different approach consists in the use of a slanted lattice, where the function $\epsilon(x, y, z)$ is offset by half of a lattice step in every direction.

Consider a cell of the lattice centered in (x, y, z), at its center the potential $\varphi(x, y, z)$ is defined. One can thus integrate Maxwell's equation on such a cell, leading to

$$\iiint_{\text{cell}} dV\ \nabla \cdot (\epsilon \nabla \varphi) = -\iiint_{\text{cell}} dV \rho$$

Using Gauss's theorem on the left hand side and the definition of charge density on the right the above expression can be written as

$$\iint_{\text{cell surface}} \epsilon \nabla \varphi \cdot d\vec{S} = Q$$

where Q is the charge inside of the cell. At this point, it is possible to separate the integral of each face and compute them separately. As an example, the face with normal equal to $+\hat{z}$ is

considered:

$$\iint_{S_{+\hat{z}}} \epsilon \nabla\varphi \cdot d\vec{S} = \iint_{S_{+\hat{z}}} \epsilon \nabla\varphi \cdot \hat{z} dS = \iint_{S_{+\hat{z}}} \epsilon \frac{\partial\varphi}{\partial z} dS$$

A simplifying assumption can be performed: the derivative of the potential can be considered constant on the surface of the cell, this is true in the case of a sufficiently fine lattice. The derivative is thus approximated using one of the expressions just discussed, leading to

$$\iint_{S_{+\hat{z}}} \epsilon \frac{\partial\varphi}{\partial z} dS \approx \frac{\varphi(z+1) - \varphi(z)}{h_z} \int_{x-\frac{h_x}{2}}^{x+\frac{h_x}{2}} dx \int_{y-\frac{h_y}{2}}^{y+\frac{h_y}{2}} dy \; \epsilon(x,y,z)$$

The last integral can be approximated using the average of the four values taken by ϵ on the edge of the surface, thus resulting in

$$\iint_{S_{+\hat{z}}} \epsilon \nabla\varphi \cdot d\vec{S} \approx h_x h_y \frac{\bar{\epsilon}(x,y,z)}{4} \frac{\varphi(z+1) - \varphi(z)}{h_z}$$

where $\bar{\epsilon}$ is the average of ϵ on the vertices of $S_{+\hat{z}}$. An indentical computation can be performed for the six sides of the cube, leading to the discretized version of the expression. A comparison between these two formulation will be presented in the next section.

An equation completely analogous to the two expressions above can be written for each cell of the box that is not fixed at a given value by a boundary condition. A completely equivalent way of expressing the above set of equations is as a linear system

$$A\vec{\Phi} = \vec{b}$$

where $\vec{\Phi}$ is a vector containing all the potentials of each cell, $\vec{b}$ contains the right hand side part, so the charge of the corresponding cell divided by its volume. The matrix A can be constructed row by row using the elements given by the above equation. All the entries will be zero apart from the ones of the cell itself and its neighbours. For example, for the first type of discretization, using of equation 5.1, the matrix element corresponding to $\varphi(x+1)$ for cell (x,y,z) will be

$$\frac{\epsilon(x+1) - \epsilon(x-1)}{4h_x^2} + \frac{\epsilon}{h_x^2}$$

and the diagonal element will be

$$-2\epsilon\left(\frac{1}{h_x^2}+\frac{1}{h_y^2}+\frac{1}{h_z^2}\right)$$

Some cell, though, will need to be at a fixed potential given by the boundary conditions. This can be performed by setting as non-zero only the diagonal element of matrix A to 1 and then the corresponding element of $\vec{b}$ to the boundary value. In this way the equation corresponding to that row in the linear system will become

$$\varphi(x,y,z) = \text{boundary value}$$

Now, in order to easily build the matrix and to then read the solution, a rule pairing the index $\vec{\Phi}$ to its corresponding cell site (x,y,z) is needed. An easy expression is the following

$$\text{index} = x + yn_x + zn_yn_x$$

This allows an easy computation of the index of neighbouring cells, for example the $z+1$ neighbour can be obtained by increasing the index by n_yn_x. A similar thing can be performed for x and y neighbours.

The issue at this point is the following: for a reasonably sized lattice, for example $100 \times 100 \times 100$, 10^6 cell are needed. This will make A a matrix with 10^{12} elements. If each element is represented with a single precision floating point value it will need roughly $8\ \mathrm{TB}$ of storage, a clearly impractical value for such a computation. This method of storage, where all the elements are saved, is the so-called dense representation. In the case shown, though, a far more efficient way is possible if one notices that the matrix is sparse. In fact, each line has only at most seven non-zero entries (the cell plus its six neighbours). If only these non-zero values are stored, together with indexes allowing to find their row and column position in A, will lead to a much more reasonable size of around $70\ \mathrm{MB}$.

Several libraries that allow this kind of computation exist, for this work the GSL (GNU Scientific Library) was chosen. After building the matrix in the so-called COO (COOrdinate) format, where three arrays are used, one for the matrix element value and the other two for its row and column index, it was converted in the CSC (Compressed Sparse Column) format. This format was chosen because it simplifies the computation of matrix-vector products that will be needed in the later stage of this simulation. This format consists of three arrays, one

containing the matrix element, one with the row index, and a third with a column pointer. If the i-th element of this last array is accessed, it will point to the position in the other two arrays where the i-th column is stored. In this way, random column access can be performed, allowing for a fast matrix-vector product.

Once both the matrix A and the source vector $\vec{b}$ are ready, the program calls the function `gsl_splinalg_itersolve_gmres` of the GSL library is called. This implements the Generalized Minimum Residual Method (GMRES), an iterative method that allows to solve sparse linear equations. Starting from an initial guess $\vec{\Phi}_0$, the residue $\vec{r}_0 = A\vec{\Phi}_0 - \vec{b}$ is computed. From it, the Krylov subspace is computed with a given number m of vectors

$$\mathcal{K}_m \equiv \text{span}(\vec{r}, A\vec{r}, A^2\vec{r}, ..., A^{m-1}\vec{r})$$

At this point, the vector with that minimises the norm of the r vector in $\mathcal{K}_m$ is computed. If a value of m equal to the dimension of the matrix is chosen, then the algorithm returns the exact solution. In this simulation a value of $m = 10$ was chosen, as it represents a value that allows the algorithm to converge at a reasonable rate.

The algorithm stops when the residue reaches a given tolerance value, i.e.

$$\frac{||\vec{b} - A\vec{\Phi}||}{||\vec{b}||} < \text{tolerance}$$

5.7 Simulation consistency with known systems

In order to test that the simulation described in the previous section works a consistency check with an analytically solvable case is shown. The geometry consists of a grounded box $1\ \text{m}$ long in the x and y directions, while it is $1\ \text{cm}$ thick in the z direction. Each direction was discretized in 100 bins. The box was divided into two halves on the z axis, with different relative dielectric constants equal to four in the lower half and one in the upper half. Two parallel planes, one at $0.4\ \text{cm}$ and the other at $0.6\ \text{cm}$ are set respectively at $\pm 1\ \text{V}$. The simulation was run until a tolerance of 10^{-3} was reached.

In figures 5.1 and 5.2 one can see the result of the simulation compared with the analytical case. There is clear agreement outside of the two planes, while inside of the capacitor the two discretization schemes show two very different behaviours. The first one exposed in the previous section, where the derivatives were directly substituted with their discretized expression, clearly disagrees with the analytical solution. The reason for this is the behaviour

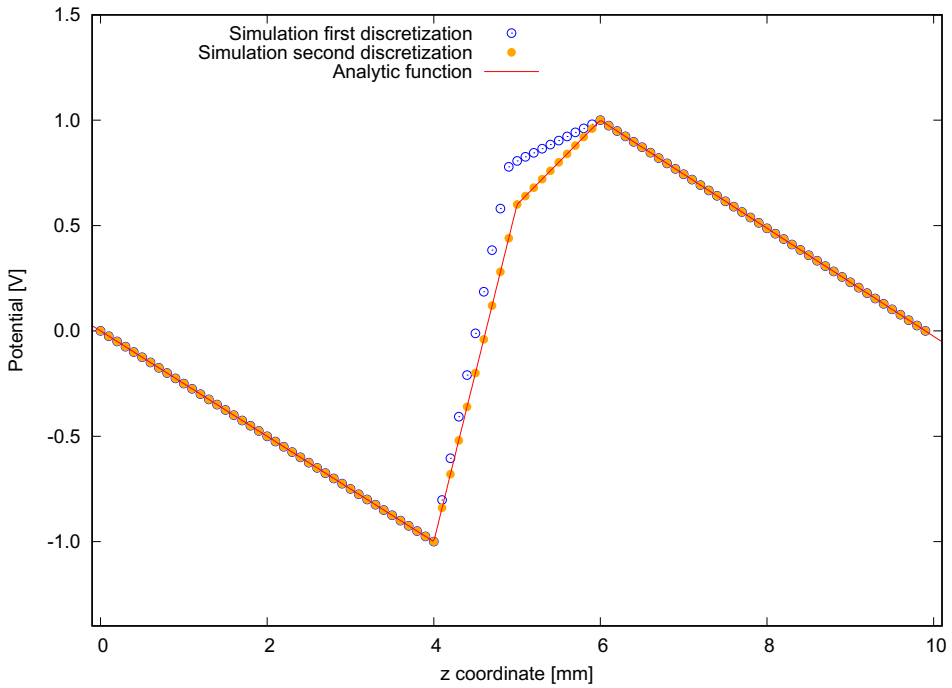

Figure 5.1: Comparison of the potential for the parallel plane capacitor between the two discretization methods and the analytical model.

of the discrete equation on the boundary between the two dielectrics. From Maxwell's equations, it is possible to show that the component of the $\vec{D}$ field normal to the surface must be conserved. This translates to the condition that

$$\epsilon_1 E_1^{\perp} = \epsilon_2 E_2^{\perp}$$

for a boundary between two regions 1 and 2. If this situation is written using the discretized equations only the second kind of procedure enforces this condition. Thus, for the following simulation, only such expressions will be used.

5.8 Simulation of the ERAM detector

A first simulation of the ERAM detector was carried out. To allow a faster computation time, a 10×10 cm^2 detector was studied. The boundary of the box was grounded, in this way the top and bottom boundaries are respectively the mesh and the pad plane. A thickness of 253 µm was set on the other axis, the lower 125 µm of which are the insulating plane, with a relative dielectric constant of 3.2, while the remaining part is set to be the 128 µm

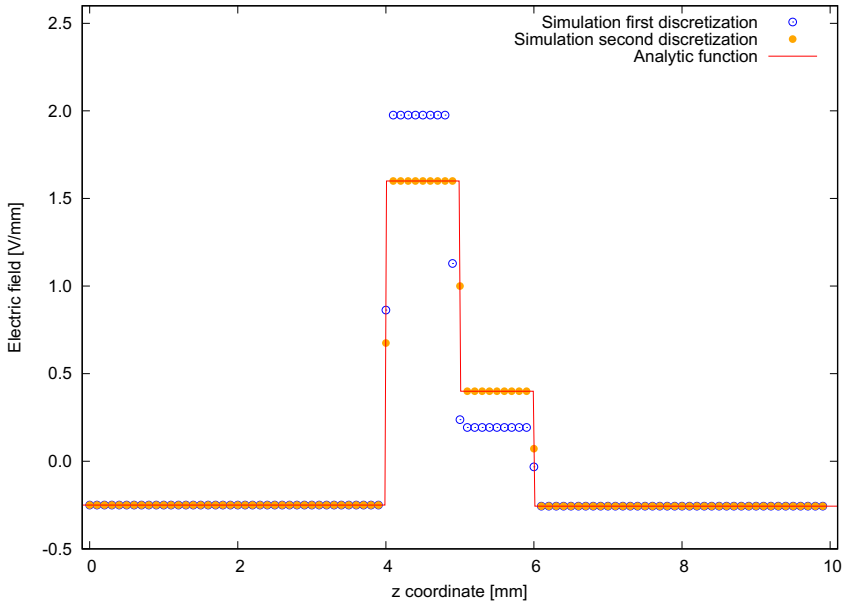

Figure 5.2: Comparison of the electric field for the parallel plane capacitor between the two discretization methods and the analytical model.

amplification gap with dielectric constant of one. On the drift direction (z-axis) the step was set to $1\ \mu\text{m}$, while it was $1\ \text{mm}$ on the other. See figure 5.3 for a schematic.

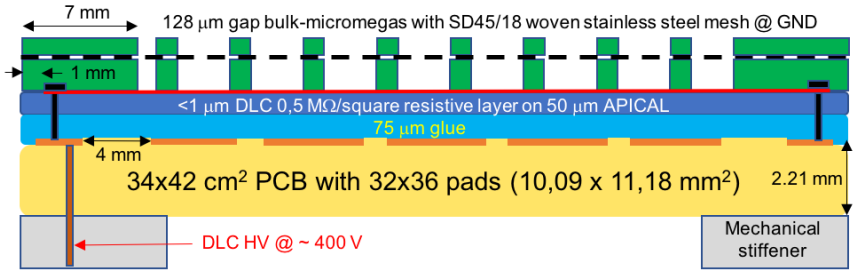

Figure 5.3: Schematic drawing of the ERAM detector simulated. Notice that only the parte between pad and mesh modelled. Courtesy of CEA IRFU of Saclay.

The DLC sheet was set with a sheet resistance of $500\ \text{k}\Omega/\square$. After the solution of the electrostatic equation with the method of the previous section was carried out, the charge on the DLC was updated. Using the 2D continuity equation

$$\frac{\partial q}{\partial t} = \frac{1}{R_S}\nabla^2_{\text{2D}}\,\varphi$$

after its discretization, the rule for updating the charge in each cell of the DLC is

$$\Delta Q = \frac{\Delta t \; h_x h_y}{R_S} \left(\frac{\varphi(x+1) - 2\varphi + \varphi(x-1)}{h_x^2} + \frac{\varphi(y+1) - 2\varphi + \varphi(y-1)}{h_y^2} \right)$$

The factor $\Delta t \; h_x h_y$ is obtained when the right hand side is multiplied by the time step and by the area of the cell, in this way converting it to a charge value.

Whereupon the source vector is updated with the new charge value and the eventual new position of the ion or some changed boundary conditions. Then the system is solved, the charge is updated and so on, until the required time is reached.

What is left to do now is to compute the charge induced on the pad plane in order to obtain meaningful information like the signal. This is achieved by using the well known fact in electrostatic that the electric field at the surface of a conductor is linked to the surface charge by the relation

$$E_{\text{surface}}(\vec{x}) = \frac{q(\vec{x})}{\epsilon}$$

So what is left to do is to compute such an electric field. On the boundary of the box, though, the symmetric derivative shown in section 5.6 on page 36 cannot be used. Instead the following can be used

$$\frac{df}{dx} = \frac{-3f(x) + 4f(x+1) - f(x+2)}{2h_x} + O(h_x^2)$$

that allows to keep the second order error.

5.9 Simulation output analysis

The above geometry was tested with two different charge configurations in order to gain insight on the validity of the 2D Telegraph equation and on the effect of the ions. The first scenario used a charge of 10^3 times the electron's one deposited at the center of the DLC layer. This allows to study the spread of a point-like charge. Such a value was chosen because, given the gain of around 10^3 of the ERAM detector, it corresponds to the amplified charge of a single primary electron.

For the second scenario, a charge with opposite sign but equal magnitude was added above the DLC layer and drifted to the mesh with a velocity of $\approx 360 \text{ m/s}$. This value was chosen because it is of the order of magnitude of the ion drift velocity for the field in the gap. This

simulation allows to study the effect that ions have on the charge spread in the DLC layer.

The first step of the analysis was to compute the standard deviation of the charge distribution over time. To do so, a slice of the distribution was taken, and each cell was weighted with the absolute value of the charge present

$$s^2 \equiv \frac{1}{Q_{\text{TOT}}} \sum_i |Q_i|(x_i - \bar{x})^2$$

where Q_{TOT} is the total charge in the slice, the i index runs on all the cells of the slice, x_i is the position of the center of the i-th cell, Q_i the charge in the cell and $\bar{x}$ is the average position of the charge distribution, computed as

$$\bar{x} = \frac{1}{Q_{\text{TOT}}} \sum_i |Q_i| x_i$$

The 2D Telegraph equation in the case of a point charge Q has a peculiar solution of

$$q(r,t) = Q \frac{RC}{4\pi t} e^{-r^2 \frac{RC}{4t}}$$

this is a normal distribution with standard deviation equal to

$$s_{\text{tel}} = \sqrt{\frac{2t}{RC}}$$

The standard deviation of the electron only simulation can be fit with such a formula to obtain the value of RC. The plot of the standard deviation for both the DLC and pad plane distribution, together with the fit, is shown in figure 5.4.

The RC value results equal to $0.1469 \pm 0.0002 \ \text{s/m}^2$. There is moreover a clear agreement between the three curves. Notice, though, how for time values lower than about $20 \ \text{ns}$ the pad standard deviation is clearly larger than the one on the DLC. This is due to the fact that the induced charge is not perfectly mutual, but rather has a distribution.

In order to better understand this aspect, consider the well known case of the charge induced on an infinite perfectly conducting plane by a nearby charge Q at distance z

$$q(r) = -Q \frac{z}{2\pi(z^2 + r^2)^{3/2}}$$

The FWHM (Full Width at Half Maximum) of such a distribution is approximately $0.766 \cdot z$,

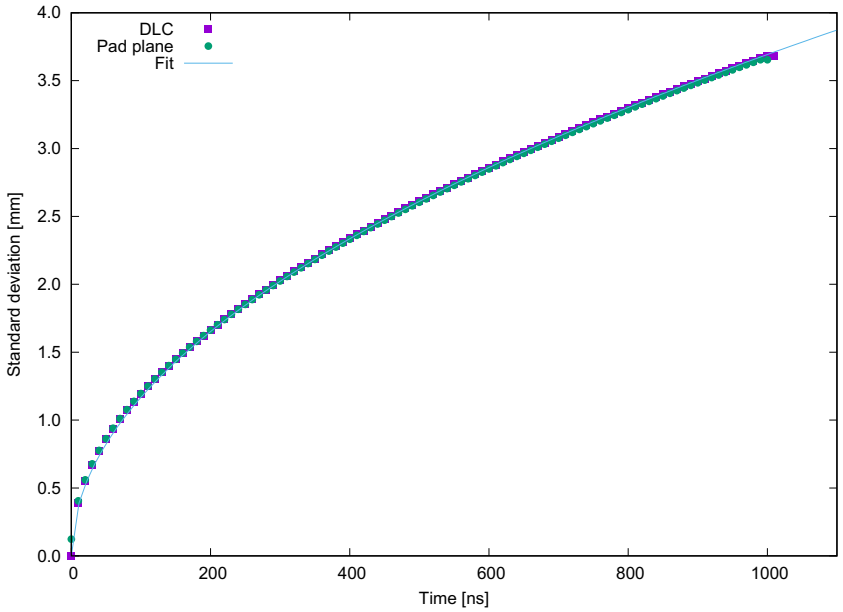

Figure 5.4: Graph showing the standard deviation of the charge distribution on the pad plane, the DLC layer and the Telegraph equation fit.

so it is possible to say that the standard deviation $s \approx 2 \cdot \text{FWHM} \approx 0.2$ mm. This value is of similar order of magnitude to the discrepancy of the initial point.

The capacitance C from the DLC point of view can be calculated as the parallel of the capacitance to the mesh and the one to the pad plane

$$C = C_{\text{mesh}} + C_{\text{pad}} = \frac{\epsilon_0 \epsilon_r}{d_{\text{mesh}}} + \frac{\epsilon_0 \epsilon_r}{d_{\text{pad}}} \approx 300 \text{ nF/m}^2$$

that gives an RC value of 0.1485 s/m^2. Such a value is of the same order of magnitude to the one obtained by the simulation, and they agree within 1% with the simulated value. This validates the charge spread modelled with the Telegraph equation in the case where only electrons are present.

An identical standard deviation analysis can be performed for the second simulation scenarios. The standard deviation compared the the one in the previous section is shown in figure 5.5. It is clear how the ion limit the spread of the charge. If the RC value is obtained with a fit as above, but computing it in the during the time when the spread is affected by ions, one obtains $RC = 0.3950 \pm 0.0003$ s/m^2. This value is a factor 2.7 greater than the one obtained without considering the ion contribution. To understand such a phenomena

the following toy model can be used.

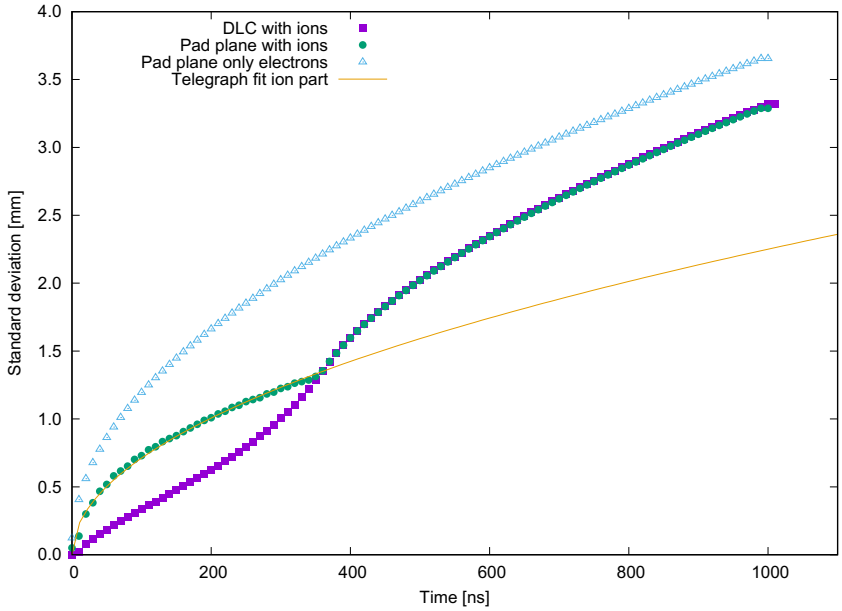

Figure 5.5: Graph comparing the standard deviation of the charge distribution on the pad plane with and without the effect of ions.

A charge Q at a distance z_0 of an infinite conducting plane is considered. The potential in such a condition is easy to compute and is given by the potential of the charge itself and of its image, thus giving

$$\varphi(r,z) = \frac{Q}{4\pi\epsilon}\left(\frac{1}{\sqrt{r^2+(z-z_0)^2}} - \frac{1}{\sqrt{r^2+(z+z_0)^2}}\right)$$

This can be used to compute the radial component of the electric field, by the appropriate component of the gradient

$$E_r(r,z) = \hat{r}\cdot(-\nabla\varphi) = -\frac{\partial\varphi}{\partial r} = \frac{Q}{4\pi\epsilon}\left(\frac{r}{(r^2+(z-z_0)^2)^{3/2}} - \frac{r}{(r^2+(z+z_0)^2)^{3/2}}\right)$$

If this function is plotted, as in figure 5.6, it will show a peculiar behaviour: it has the same long distance magnitude of the one of an equal charge in the DLC layer. These electric fields will thus eliminate each other, in this way limiting the long distance effects and functionally slowing the rate of diffusion while the ion drift is present. This sizable *shepherd dog effect* will need to be taken into account in the future models of charge spread, as it impacts the

RC value that might be obtained during the characterization of the detector.

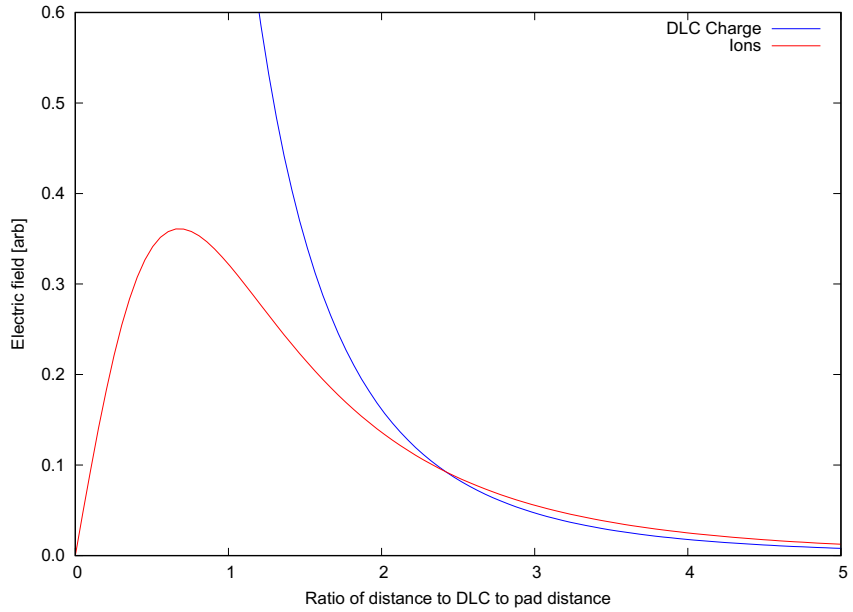

Figure 5.6: Comparison of the modulus of the radial component of the electric field for a charge on the DLC and an ion at a distance double the one between pad and DLC from the pad plane.

An additional consistency check that is needed to validate the simulation is to compare the induced charge with an analytic model. Using the simulation with the ion, the induced charge on the pad plane was computed and compared with the one expected from Shockley-Ramo theorem, corrected in the case of dielectrics. The result is shown in figure 5.7.

The interpretation of the induced charge is the following: at $t = 0$ the ions and electrons are in the same position, so their net charge is zero, thus there is no induced charge. As the ions start to migrate, they induce less charge on the pad plane, thus the induction effect of electrons prevails. At around $t \approx 350$ ns the ions reach the mesh and are neutralized, leaving only the induced charge of the electrons on the DLC.

5.10 Shepherd dog effect in the 2D telegraph equation

The shepherd dog effect can be included in the 2D telegraph equation if it is assumed that the motion of the ions is not affected by the charge distribution on the DLC. This can be considered the case due to the strong electric field in the amplification gap. In section 5.4 on

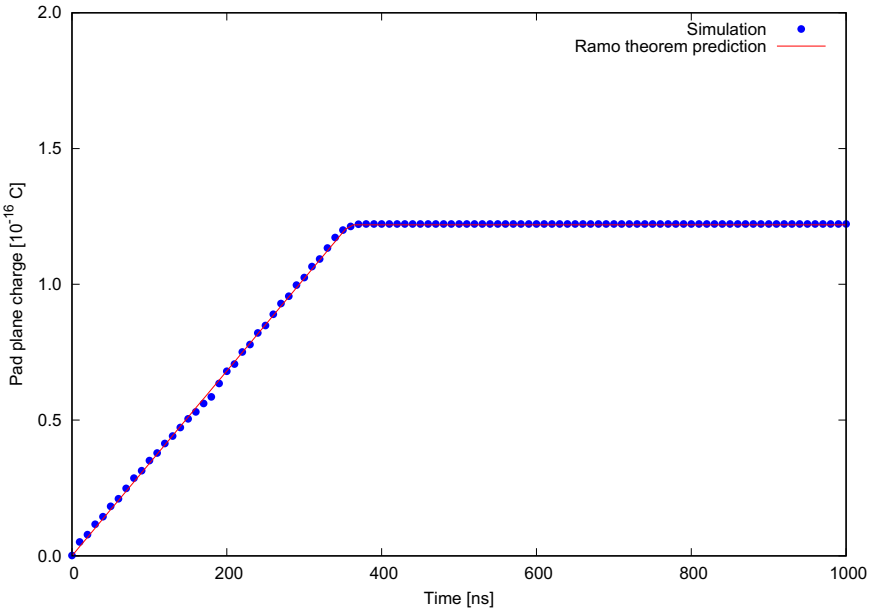

Figure 5.7: Comparison of the expected induced charge on the pad plane using the simulation and the analytic result of Ramo theorem.

page 33 it was shown that

$$\frac{\partial q}{\partial t} = \frac{1}{R_S} \nabla^2_{\text{2D}} \, \varphi$$

where q is the charge density, φ the potential and R_S the sheet resistance. Such a formula holds in the general case and yields the 2D telegraph equation if $q = C\varphi$ is assumed.

The potential can be written as the sum of two components sourced respectively by the ions in the amplification gap and by the electrons in the DLC. In this way it is possible to write

$$\varphi = \varphi_{\text{DLC}} + \varphi_{\text{ion}} = \frac{q}{C} + \varphi_{\text{ion}}$$

The potential of the ion, though, is not affected by q in any way, thus the corresponding component can be used as a source term in the differential equation

$$\frac{\partial q}{\partial t} = \frac{1}{R_S C} \nabla^2_{\text{2D}} \, q + \frac{1}{R_S} \nabla^2_{\text{2D}} \, \varphi_{\text{ion}}$$

The computation of φ_{ion} is critical. The first idea that might come to mind is the analytic solution of the electrostatic equation for the ions in the desired geometry. In the resistive MICROMEGAS case under study it is not trivial.

To avoid such a calculation, one might use again the idea of the infinitesimal capacitor approximation already used for the telegraph equation. This time, though, a virtual floating conductor is placed in the position of the ion and has the ion's charge deposited on it. As shown in the schematic of figure 5.8, it is possible to obtain the potential on the DLC for an ion charge density q_{ion} at height z by solving the capacitive divider. This results in

$$\varphi_{\text{ion}} = \frac{q_{\text{ion}}}{C_{\text{TOT}}} \frac{C_{\text{PAD-z}}}{C_{\text{DLC-PAD}}}$$

that, using the expressions for the parallel plane capacitor, becomes

$$\varphi_{\text{ion}} = \frac{q_{\text{ion}}}{\epsilon_0} \frac{1}{1 + \frac{\frac{b}{\epsilon_r} + z}{g - z}} \frac{b}{\epsilon_r}$$

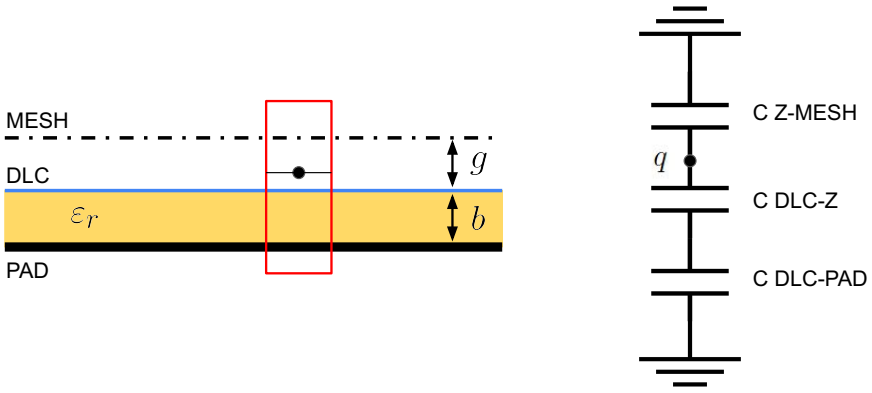

Figure 5.8: In the capacitor approximation each section of the ERAM with its charge distribution can be viewed as a separate capacitor divider. If the charge moves out of plane, the capacitances are not constant.

Using this expression requires great care. In fact, q_{ion} is a Dirac delta function and thus its laplacian is not a trivial mathematical concept. In order to better understand the proper way to setup this problem, consider the case of the diffusion of a point charge Q starting at the origin at $t = 0$. A way to see this problem is to use the Green's function properties. The point charge is originated by an impulsive current at the origin, namely

$$i(x, y, t) = Q\, \delta(x)\, \delta(y)\, \delta(t)$$

Notice how this is dimensionally a variation of charge density per unit time.

The Green function for the telegraph equation is

$$G(x,y,t,x',y',t') = \theta(t-t')\,\frac{1}{4k\pi(t-t')}\,e^{-\frac{(x-x')^2+(y-y')^2}{4k(t-t')}}$$

where $k = (RC)^{-1}$.

The solution for the above current is then obtained as

$$\begin{aligned} q(x,y,t) &= \int_{-\infty}^{+\infty} dx' \int_{-\infty}^{+\infty} dy' \int_{-\infty}^{+\infty} dt'\; G(x,y,t,x',y',t')\, i(x',y',t') \\ &= \int_{-\infty}^{+\infty} dx' \int_{-\infty}^{+\infty} dy' \int_{-\infty}^{+\infty} dt'\; \theta(t-t')\,\frac{Q}{4k\pi(t-t')}\,e^{-\frac{(x-x')^2+(y-y')^2}{4k(t-t')}}\,\delta(x')\,\delta(y')\,\delta(t') \\ &= \theta(t)\,\frac{Q}{4k\pi t}\,e^{-\frac{r^2}{4kt}} \end{aligned}$$

due to the properties of the Dirac delta function. As it is clear, the well known solution already described is obtained.

When the ions are present, though, the situation changes. On the ohmic sheet there will be no net charge at $t = 0$, due to the equal and opposite charges of electrons and ions. When the ions start to drift, the charge is weighted with the z dependent factor shown in equation 5.10. This is equivalent to the appearance of negative charge at a rate governed by such a factor. In this case the current expression will be

$$i(x,y,t) = \begin{cases} Q\,\delta(x)\,\delta(y)\,\dfrac{d}{dt}\left(\dfrac{1}{1+\frac{\frac{b}{\epsilon_r}+z(t)}{g-z(t)}}\right) & \text{for } 0 < t < T \\ 0 & \text{otherwise} \end{cases}$$

If a motion in the insulation gap with constant velocity taking a time T to reach the mesh is considered, then

$$z(t) = g\frac{t}{T}$$

So the current becomes

$$i(x,y,t) = \begin{cases} -Q\,\delta(x)\,\delta(y)\,\dfrac{1}{T(1+m)} & \text{for } 0 < t < T \\ 0 & \text{otherwise} \end{cases}$$

where $m \equiv \frac{b}{g\epsilon_r}$

When this expression is convoluted with the Green's function, this leads to

$$q(r,t) = Q \begin{cases} \dfrac{\mathrm{Ei}\left(-\frac{r^2}{4kt}\right)}{4\pi kT(m+1)} & \text{for } 0 < t < T \\ \dfrac{\mathrm{Ei}\left(-\frac{r^2}{4kt}\right) - \mathrm{Ei}\left(-\frac{r^2}{4k(t-T)}\right)}{4\pi kT(m+1)} & \text{for } t > T \end{cases}$$

where $\mathrm{Ei}(x)$ is the exponential integral function defined as

$$\mathrm{Ei}(x) = \int_{-\infty}^{x} \frac{e^t}{t}\,dt$$

A graph of the solutions in the two regimes for t smaller and greater than T are shown in figure 5.9. The two curves show a very different behaviour. When t is smaller than T, there is a divergence at the origin, this is compatible with the expected behaviour of having a delta-like current injected there. Moreover, a tail is clearly visible, due to the spread of the charge injected previously. Afterwards, when t is greater than T, the divergence disappears, leaving a bell-shaped distribution.

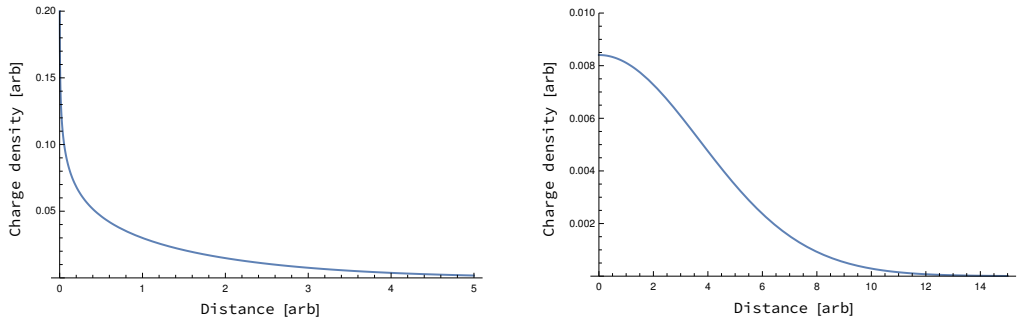

Figure 5.9: On an example of the charge distribution when $t < T$, while on the right $t > T$.

It is now possible to calculate observables that can be compared with the simulation, in

order to validate this method. As shown in the previous section, the standard deviation of a slice was computed. This can also be computed analytically as

$$s^2(t) = \frac{\int_0^{+\infty} dr\ r^2\, q(r,t)}{\int_0^{+\infty} dr\ q(r,t)}$$

Notice how in the above expression no jacobian is present, even though the charge density is defined in polar coordinates. This is due to the fact that a projection, for example on x, is taken.

If the above calculation is performed in the case of a point charge the usual result of

$$s^2_{\text{no ion}}(t) = \frac{2t}{RC}$$

is obtained. In the case just described, on the other hand, this leads to

$$s^2_{\text{shepherd}} = \begin{cases} \dfrac{2t}{3RC} & \text{for } 0 < t < T \\ \dfrac{2}{3RC}\left(2t + \sqrt{t(t-T)} - T\right) & \text{for } t > T \end{cases}$$

This formula reproduces well the complex behaviour predicted by the simulation, as shown in figure 5.10.

This result exhibits some interesting properties:

1. during the time when the ion affect the charge spread the RC value is increased by a factor of three;
2. this increase in RC does not depend on the geometry;
3. this increase in RC does not depend on the drift time of the ions;
4. the ion's drift time affects only the amount of time this the limited diffusion occurs.

To confirm these properties an additional simulation with slower drift speed ($200\ \mathrm{m/s}$) was performed, the result is shown in figure 5.10. It is clear that the result of the two simulations exhibit an identical behaviour in the period of time where ions directly affect the charge spread, as predicted by the analytical model.

Moreover, notice how for $t \gg T$ the standard deviation recovers the behaviour of the charge spread without ions.

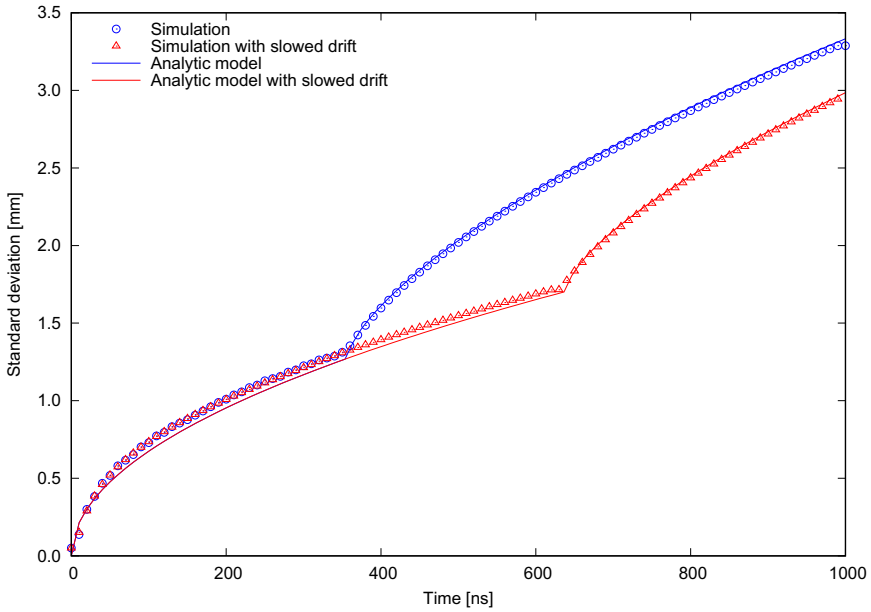

Figure 5.10: Comparison of the simulation shown in the previous section with another with slower ions and with the prediction of the analytic formula just described.

5.11 Tracks in the 2D telegraph equation

Another interesting case to analyze is the one of a straight track with a linear charge density equal to λ. In the case where the effect of ions are neglected, the external source current can be written as

$$i(x, y, t) = \lambda\, \delta(x)\, \delta(t)$$

in the case of a straight track located on top of the y axis. This is identical to the one of the point charge, except there is a constant density along the track.

The convolution with Green's function gives

$$\begin{aligned} q(x, y, t) &= \int_{-\infty}^{+\infty} dx' \int_{-\infty}^{+\infty} dy' \int_{-\infty}^{+\infty} dt'\; \theta(t - t')\, \frac{\lambda}{4k\pi(t - t')}\, e^{-\frac{(x-x')^2+(y-y')^2}{4k(t-t')}}\, \delta(x')\, \delta(y')\, \delta(t') \\ &= \theta(t)\, \frac{\lambda}{4k\pi t} \int_{-\infty}^{+\infty} dy'\, e^{-\frac{x^2+(y-y')^2}{4kt}} \\ &= \theta(t)\, \frac{\lambda}{2\sqrt{\pi k t}}\, e^{-\frac{x^2}{4kt}} \end{aligned}$$

The standard deviation of a slice along the x-axis can be computed as discussed in the

previous section, resulting in

$$s^2 = \frac{2t}{RC}$$

In the same way as in the previous section, the source term with the effect of ions can be expressed as

$$i(x,y,t) = \begin{cases} -\lambda\,\delta(x)\,\dfrac{1}{T(1+m)} & \text{for } 0 < t < T \\ 0 & \text{otherwise} \end{cases}$$

where the last factor comes from the the fact that the ion's movement is "showing" the charge of the electron.

The convolution with the Green's function gives

$$\begin{aligned} q(x,y,t) &= -\int_{-\infty}^{+\infty} dx' \int_{-\infty}^{+\infty} dy' \int_0^T dt'\; \theta(t-t')\,\frac{1}{4k\pi(t-t')}\,e^{-\frac{(x-x')^2+(y-y')^2}{4k(t-t')}}\,\frac{\lambda\,\delta(x)}{T(1+m)} \\ &= -\int_0^T dt'\;\frac{\lambda}{T(1+m)}\,\theta(t-t')\,\frac{1}{4k\pi(t-t')}\,e^{-\frac{x^2}{4k(t-t')}}\int_{-\infty}^{+\infty} dy'\,e^{-\frac{(y-y')^2}{4k(t-t')}} \\ &= -\frac{\lambda}{2T(1+m)}\int_0^T dt'\;\theta(t-t')\,\frac{e^{-\frac{x^2}{4k(t-t')}}}{\sqrt{\pi k(t-t')}} \end{aligned}$$

This integral is not trivial to evaluate. To do this first it is necessary to understand the effect of the Heaviside theta function. Notice how, if $t < T$, the values of such that $t < t' < T$ will make the it vanish. In this way it is possible to write

$$\int_0^T dt'\;\theta(t-t') \to \int_0^{\min\{t,T\}} dt'$$

At this point, using the definition of the incomplete gamma function

$$\Gamma(s,x) \equiv \int_x^{+\infty} z^{s-1}\,e^{-z}\,dz$$

and performing the substitution

$$z = \frac{x^2}{4k(t-t')}$$

the integral is evaluated as

$$q(x,y,t) = \frac{\lambda x}{4kT(m+1)\sqrt{\pi}} \begin{cases} \Gamma\left(-\frac{1}{2}, \frac{x^2}{4kt}\right) & \text{for } 0 < t < T \\ \Gamma\left(-\frac{1}{2}, \frac{x^2}{4kt}\right) - \Gamma\left(-\frac{1}{2}, \frac{x^2}{4k(t-T)}\right) & \text{for } t > T \end{cases}$$

It is now possible to evaluate the standard deviation of a slice along the x-axis that results equal to

$$s^2_{\text{shepherd}} = \begin{cases} \frac{2t}{2RC} & \text{for } 0 < t < T \\ \frac{2}{RC}\left(t - \frac{T}{2}\right) & \text{for } t > T \end{cases}$$

This result shows that a different behaviour emerges in this case. The new "effective" RC value gains a factor of two with respect to the case where ions are not taken into account, while the usual spread is recovered when this effect is removed.

6

Model comparison with data

6.1 The signal induced in a MICROMEGAS

In the previous chapter a model of the charge spread of electrons in the ohmic sheet inside of an ERAM detector with and without the effect of ions was presented. It is now interesting to use this information to predict the signal observed in the detector.

To calculate the charge induced on a pad the analytic solutions have to be integrated over the pad area. In that case, we consider a pad with sides along the x and y axis respectively l_x and l_y long, with its center at distance d from the track. Given the translational symmetry along the y, the integration on the y axis gives simply a factor of l_y, so the charge induced on the pad at any time can be written as

$$Q(t) = l_y \int_{d-\frac{l_x}{2}}^{d+\frac{l_x}{2}} q(x,t)\, dx$$

In the next section it will be shown how the actual observable needed is the current $I(t)$, the derivative of $Q(t)$. It is important to notice, however, how in the case with ions it is much simpler to first compute the derivative of $q(x,y,t)$ and then integrate it. This computation in the case without ions leads to

$$I(t) = \frac{k\lambda l_y}{8\sqrt{\pi}(kt)^{3/2}} \left((2d - l_x) e^{-\frac{(l_x-2d)^2}{16kt}} - (2d + l_x) e^{-\frac{(2d+l_x)^2}{16kt}} \right)$$

This formula shows an interesting behaviour with varying distance from the track, as it is clear from figure 6.1. The leading pad, i.e. the one actually containing the charge, has a strictly negative current, while the neighbouring one has a positive current. This phenomena can be explained as follows: the leading pad contains some charge, that diffuses away, while the neighbouring pad gains charge. Notice however, that the signal becomes negative also for the neighbouring pad. This can be seen algebrically: when t goes to infinity, the exponentials tend to one. This leaves a factor

$$(2d - l_x)e^{-\frac{(l_x-2d)^2}{16kt}} - (2d + l_x)e^{-\frac{(2d+l_x)^2}{16kt}} \xrightarrow{t\to+\infty} -2l_x$$

This makes the current negative at very long times, when the charge is escaping its initial position.

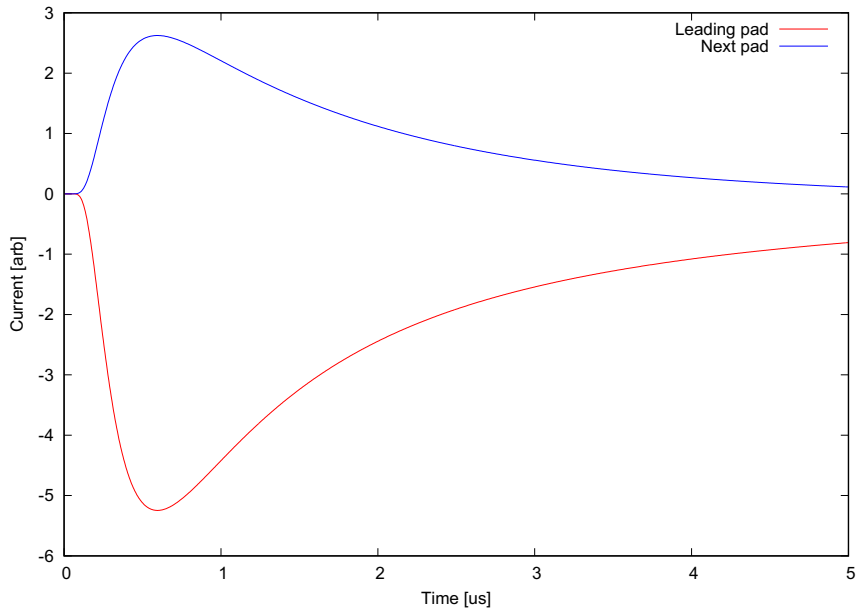

Figure 6.1: Comparison between the signal of the leading and neighbouring pad.

While, in the case with ions

$$I(t) = \sqrt{\frac{\pi}{2}}\frac{\lambda l_y}{2(m+1)T}\left(\text{erf}\left(\frac{l_x - 2d}{4\sqrt{kt}}\right) + \text{erf}\left(\frac{2d + l_x}{4\sqrt{kt}}\right)\right)$$

for $0 < t < T$ and

$$I(t) = \sqrt{\frac{\pi}{2}} \frac{\lambda l_y}{2(m+1)T} \left(-\text{erf}\left(\frac{l_x - 2d}{4\sqrt{k(t-T)}} \right) - \text{erf}\left(\frac{2d + l_x}{4\sqrt{k(t-T)}} \right) + \right.$$
$$\left. + \text{erf}\left(\frac{l_x - 2d}{4\sqrt{kt}} \right) + \text{erf}\left(\frac{2d + l_x}{4\sqrt{kt}} \right) \right)$$

for $t > T$.

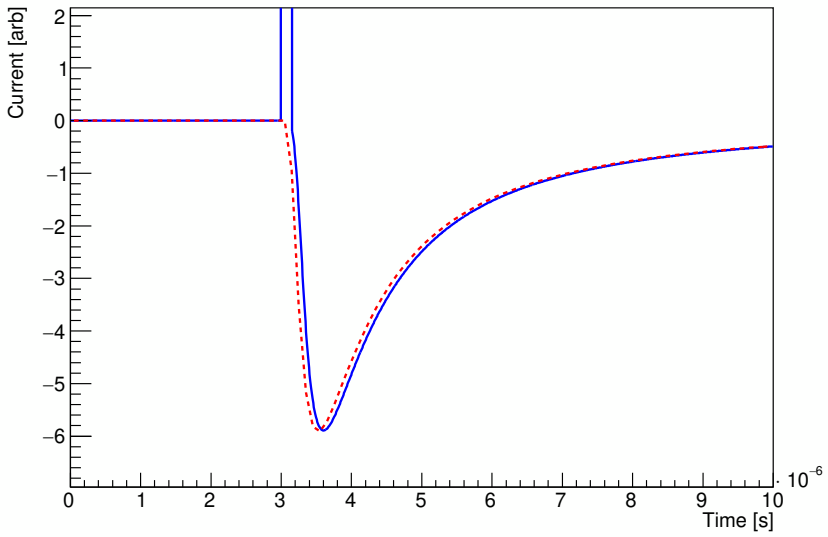

Figure 6.2: Plot of the current predicted by the two different model: with ions (solid blue line) and without ions (dashed red line).

Notice how the leading pad signal is significantly different among the two models (figure 6.2): for the case without ions only a negative current is present, while if ions are considered an initial positive current is present. This current is due to the induction of the ions. Notice that, in order to compare the model without ions with the data, it is necessary to add a positive Dirac delta in order to mimic the effect of the ions' induced charge.

6.2 Front-end electronics transfer function

The signal discussed in the previous section is not directly sampled but is first shaped with a front-end electronic chain composed of a charge sensitive preamplifier, a pole-zero cancellation stage and a filter. The Laplace transform of the transfer function can be written after

combining each of these stages

$$V_{\text{out}}(s) = I(s) \times \left(\frac{1}{C_f} \frac{-1}{s + \frac{1}{\tau_f}} \right) \times \left(-\frac{C_p}{C_s} \frac{s + \frac{1}{\tau_p}}{s + \frac{1}{\tau_s}} \right) \times \left(\frac{3}{2} \frac{1}{s^2 + \frac{3}{2}\frac{s}{\tau_s} + \frac{1}{\tau_s^2}} \right)$$
$$= I(s)\, T(s)$$

where $V_{\text{out}}(s)$ is the Laplace transform of the output signal of the electronic chain for an input current $I(s)$. τ_f is the time constant of the charge amplifier, representing the decay time of the discharge of the capacitance integrating the input current. Notice how, for big decay times where $s >> \tau_f^{-1}$, this term becomes equivalent to $1/s$, namely the integration in the Laplace domain. The finiteness of this time constant leads to the appearance of long tail to the signals, due to the discharge of the capacitor. To avoid this, the pole is simplified with a zero having $\tau_p = \tau_f$, modifying the signal time characteristic and filtering it in the next stage. In this way the electronics response has a small tail. Here $T(s)$ represents the transfer function.

Using the properties of the Laplace transform linking multiplication and convolution, one finds that

$$V_{\text{out}}(t) = \mathcal{L}^{-1}[I(s)\, T(s)](t) = I(t) \star T(t)$$

where $\star$ represents the convolution and $T(t)$ is the response of the electronic to a Dirac delta current.

The delta response of the electronics can be computed with the inverse Laplace transform of the transfer function, that in the case where $\tau_f = \tau_p$ leads

$$T(t) = 3e^{-t/\tau_s} + \frac{3}{7} e^{-3t/4\tau_s} \left(\sqrt{7} \sin\left(\frac{\sqrt{7}t}{4\tau_s} \right) - 7 \cos\left(\frac{\sqrt{7}t}{4\tau_s} \right) \right)$$

A plot of this function is visible in figure 6.3.

6.3 Mesh pulsing run

To study the transfer function of the front-end electronics a potential relative to ground was applied to the mesh of the ERAM detector. When this is done, charge is deposited on it, thus inducing a current on the underlying pads. The applied potential was a negative signal with a sharp increase followed by an exponential decay with a timing constant of 10 ms and with

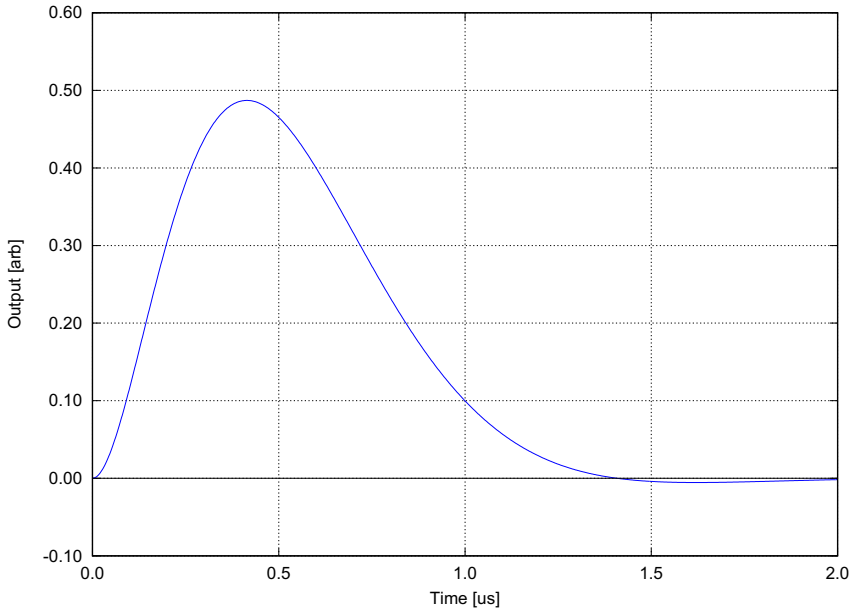

Figure 6.3: Theoretical impulse response of the AFTER chip for τ_s equal to 206 ns, roughly corresponding to a shaping time of 412 ns. The curve exhibits a small undershoot.

an amplitude in the order of 10 mV (for the 120 fC AFTER range). The signal is produced with an arbitrary function generator and the cable is terminated with a $50\ \Omega$ resistor before being applied to the mesh.

It is important, however, to consider the effect of the capacitance between the mesh and the pads. This, together with the generator output's impedance, behaves like an RC filter. Such an effect has to be added to the response function of the electronics. The capacitance between mesh and the pad plane can be computed using the infinite parallel plane capacitor approximation. For the ERAM-01 detector employed in this measurement this capacitance is equal to 5.54 nF, resulting in a time constant $\tau_{\text{mesh}} = 277$ ns.

The signal of a channel was averaged with several pulses, in order to get rid of electrical noise, and the response function amplitude and delay were fitted, while the shaping time and the τ_{mesh} were fixed. An example is shown in figure 6.4. There is clearly an agreement between the signal and the red curve. The fit of the unconvoluted response function is shown with the blue curve. It is important to notice how these two fits have the same number of degrees of freedom. Moreover, the signal is widened and the undershoot disappears.

The agreement of these two signal shapes is important: in fact, during the production process the thickness and dielectric constant of the insulation layer is not fully under control. If

a discrepancy was observed, it would mean one of this two quantities will not be the designed one. In turn, if a measurement of the RC constant of the ERAM has a strong discrepancy with the expected value, this allows to rule out a possible cause.

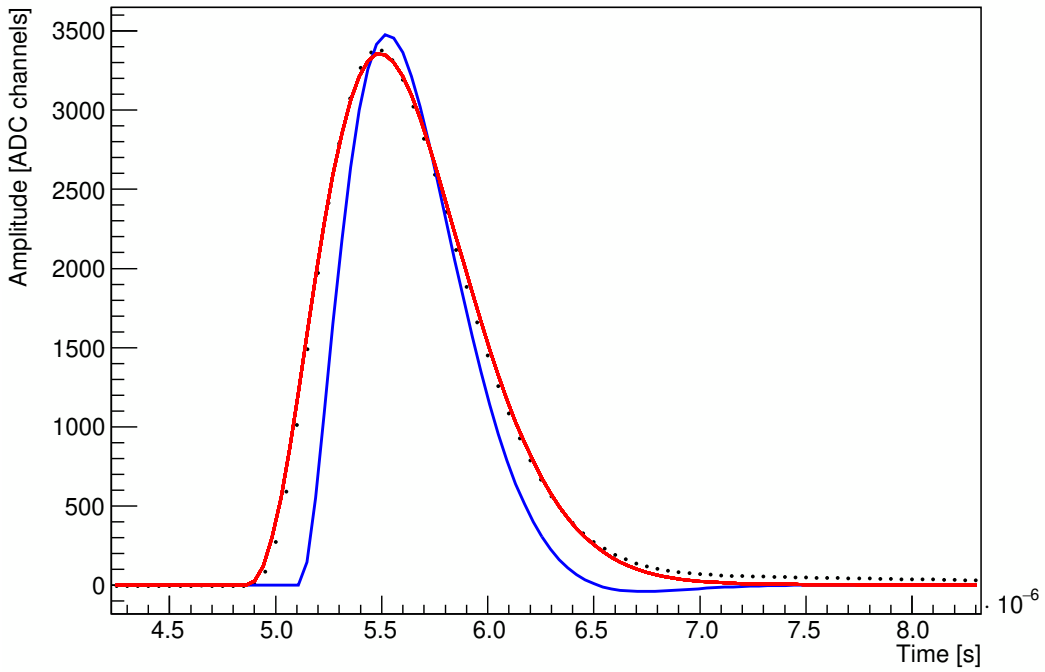

Figure 6.4: Averaged mesh pulsing signal (black dots) and fits of the response function unconvoluted (blue) and convoluted with an exponential (red).

6.4 Pad signal fit

With the techniques discussed in the previous Sections it is possible to perform a fit of the pad's waveforms in order to determine unknown parameters of the model, where the main goal is the measurement of the RC constant and of the track impact parameter with respect to the pad center.

To this purpose a dedicated data sample was collected during the DESY test beam with "zero-suppression" disabled: during the normal data taking, the TPC electronics records only those waveform portion which are above a certain threshold, plus some samples in the immediate vicinity of those regions. This "zero-suppression" mode of operation is necessary

to limit the amount data recorded to disk. Charge spread in the leading pad, though, manifests itself as an undershot that is usually not completely recorded due to zero-suppression. As a consequence, for avoiding to loose information encoded within the signal undershoot, zero-suppression has to be disabled.

The example of a non zero-suppressed event is shown in figure 6.5. The track, propagating along the horizontal direction, is the analyzed by splitting it in vertical clusters of three pads. A simultaneous fit of the three waveforms is performed by linearly combining the related χ^2s. The fitting function for each waveform is the convolution of the electronics response with the current signal, as discussed in the previous Sections. The free parameters in the fitting functions are the following: the characteristic time constant (RC), the time of arrival of the signal (t_0), the impact parameter of the track (projected on the ERAM) with respect to the center of the pad (d) and a common normalization factor A.

An example of such a fit is shown in figure 6.6.

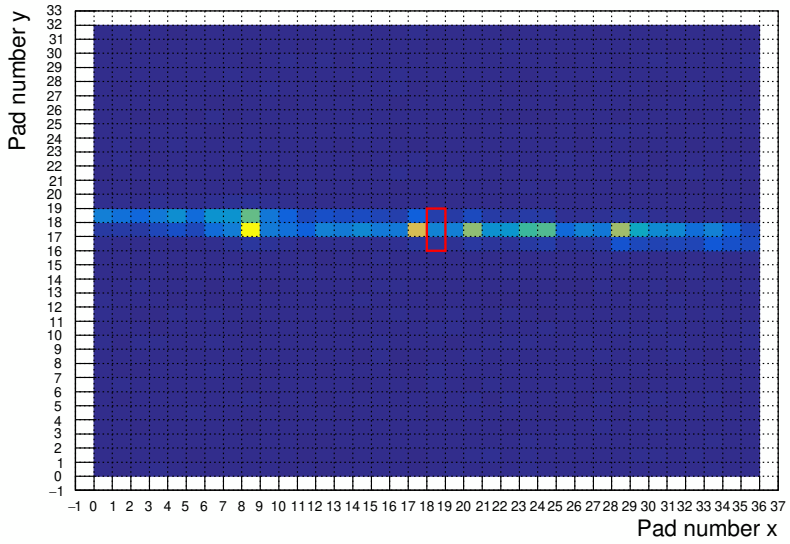

Figure 6.5: Example of electron track used in the fit. The red box shows one of the three pad clusters.

From a small statistic sample of selected tracks we estimated an average value of RC at the level of 130 ± 20 ns/mm^2. This result is in clear tension with the expected value of around 50 ns/mm^2.

Several explanations are possible, due to effects which are at the moment not accounted by the fit. The main effects that could bias the fit are the following. First, fluctuations of

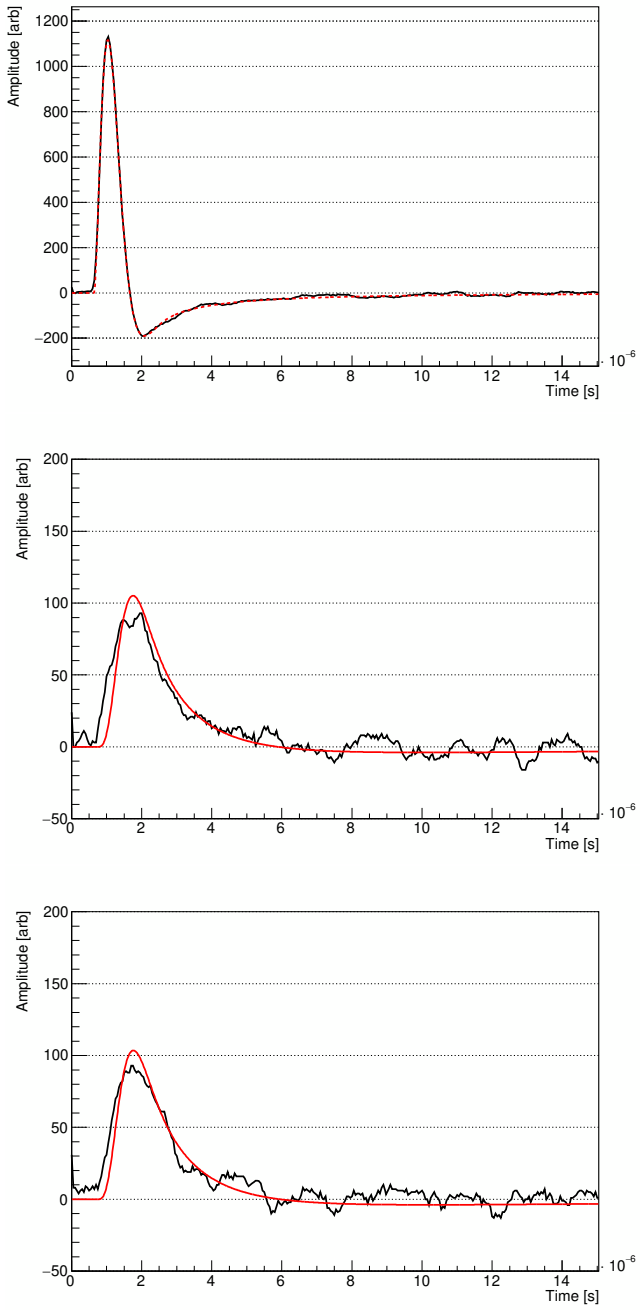

Figure 6.6: Example of fit of the signal of a pad cluster. From top to bottom the leading pad and the two neighbouring pad. The red line is the fit curve.

the primary charge produced along the track might play a role. In the case of a uniform

charge distribution along the track, the "longitudinal" charge spread along the track trajectory projected on the DLC would cancel out due to opposite, symmetrical charge spread currents. On the contrary the ionization is actually fluctuating and these effect should play a role. Additional effects which might bias the fit are space charge effects on the DLC layer (due to the long diffusion time) and non uniformity in DLC resistivity. Effects related to the electronics or abnormal DLC-pad or Mesh-DLC capacitance are ruled out by mesh pulsing measurements (see previous Section).

Biases to the fit will be studied in detail with the large statistics that are presently being collected at the DESY test beam. In addition systematical studies will be performed by illuminating the ERAM module with X-rays (from a ^{55}Fe source) and by laser ionization induced "tracks". Of course biases will be also studied with the help of Monte Carlo simulations.

Concerning the effect of ions (shepherd dog effect, see previous Chapter), it appears not to modify too much the results of the fit. Additional not zero-suppressed data are needed in order to verify the impact of the effect on the fit. An important parameter which should be studied in order to limit the number of free parameters is the ion's drift time in the amplification gap. Experimental verification of this effects will be addressed in future studies, as described in the next paragraph.

6.5 Possible experimental tests of the shepherd dog effect

Carrying out an experiment to directly show the presence of the shepherd dog effect is challenging. The goal of such a measurement would be to compare the signals seen on the pads of a MICROMEGAS when electrons spread with and without the ions. The issue is that avalanche multiplication inevitably produces electron-ion pairs, so it must be avoided if the ions' effect has to be removed.

One possibility (figure 6.7) is to use more ionizing particles, for example the Helium-4 nuclei produced in an α decay. Such a particle is about a factor of 500 more ionizing than a minimum ionizing muon. Due to the fact that the MICROMEGAS gain is of the order of 10^3, electrons produced by an α particles might be detectable without avalanche amplification.

In this way, a detectable amount of electrons can be produced already in the active volume of the TPC and be deposited on the DLC of an ERAM with low electric field in the gap, in this way observing the charge spread without the ion contribution. If, on the other hand, the α particle traverses the amplification gap, ions will be present and will affect the spread.

Comparing the two conditions an enhanced charge would clearly show the presence of the shepherd dog effect.

Technically this measurement is difficult: the source needs to be collimated in order to have an electron distribution with a reproducible shape. Moreover, placing a source in the active region of the TPC would potentially alter the electric field, thus making difficult to predict the charge transport. A transport effect might also arise from space charge effects produced by the high density of charge produced by ionization.

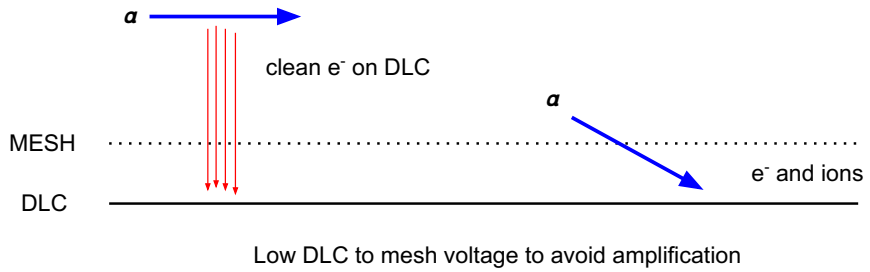

Figure 6.7: Schematic drawing of a possible experiments to test the effect of ions on the charge spread.

7 Conclusion

The study of the signal formation in the ERAM detector was presented. Specifically, using a Finite Elements simulation it was possible to validate the 2D telegraph equation for the description of the charge spread of the electrons on the resistive layer within the ERAM. In addition, the ions effect, which was previously not accounted for, was introduced showing a possibly sizable effect in limiting (delaying) the electrons spread.

The complete setup of a prototype of the HA-TPC of the T2K experiment was described, alongside the first data taking during a test beam in June 2021 at DESY, where the TPC prototype was exposed to 4 GeV$/c$ electrons. From such data, it was possible to perform a rough estimation of the characteristic charge spread time constant (RC) that was found in tension with the expected value. More work will be needed to accurately characterize the charge spread.

In particular the contributions due to the fluctuation of the numbers of primary electrons produced along the track and the their diffusion during the drift shall be addressed both with analyzing new data obtained with X-ray sources and laser induced ionization and with a full Monte Carlo simulation.

In summary, this work represents an initial attempt to accurately fit pad signals, which might be quite useful to calibrate the detector: in fact it will allow to build an RC time constant map as a function of the position on the ERAM detector, which in turn will enable very accurate track reconstruction algorithms.

References

[1] C. S. Wu et al. Experimental Test of Parity Conservation in Beta Decay. *Physical Review*, 105(4), feb 1957.

[2] P. A. Zyla and Others. Review of Particle Physics. *PTEP*, 2020(8):083C01, 2020.

[3] J. H. Christenson et al. Evidence for the 2π Decay of the K_0^2 Meson. *Physical Review Letters*, 13(4):138–140, jul 1964.

[4] Y. Fukuda et al. Evidence for Oscillation of Atmospheric Neutrinos. *Physical Review Letters*, 81(8), aug 1998.

[5] Q. R. Ahmad et al. Measurement of the Rate of $\nu_e + d \rightarrow p + p + e^-$ Interactions Produced by ^{8}B Solar Neutrinos at the Sudbury Neutrino Observatory. *Physical Review Letters*, 87(7), jul 2001.

[6] F. P. An et al. Observation of Electron-Antineutrino Disappearance at Daya Bay. *Physical Review Letters*, 108(17), apr 2012.

[7] K. Abe et al. The T2K experiment. *Nuclear Instruments and Methods in Physics Research Section A: Accelerators, Spectrometers, Detectors and Associated Equipment*, 659(1), dec 2011.

[8] K. Abe et al. T2K ND280 Upgrade – Technical Design Report. jan 2019.

[9] W. Blum et al. *Particle Detection with Drift Chambers*. 2008.

[10] G. F. Knoll. *Radiation Detection and Measurement*. Wiley, 2010.

[11] P. Baron et al. AFTER, an ASIC for the Readout of the Large T2K Time Projection Chambers. *IEEE Transactions on Nuclear Science*, 55(3), jun 2008.

[12] R. Diener et al. The DESY II test beam facility. *Nuclear Instruments and Methods in Physics Research Section A: Accelerators, Spectrometers, Detectors and Associated Equipment*, 922, apr 2019.

[13] W. Riegler. Electric fields, weighting fields, signals and charge diffusion in detectors including resistive materials. *Journal of Instrumentation*, 11(11), nov 2016.

[14] M. Dixit and A. Rankin. Simulating the charge dispersion phenomena in Micro Pattern Gas Detectors with a resistive anode. *Nuclear Instruments and Methods in Physics Research Section A: Accelerators, Spectrometers, Detectors and Associated Equipment*, 566(2), oct 2006.

Acknowledgments

Voglio sfruttare questa breve sezione per ringraziare tutte le persone che mi hanno supportato nei momenti, talora difficili, che hanno portato alla conclusione di questo lavoro. Nello specifico un ringraziamento speciale a Gianmaria, Magda e Tommaso. Non posso non menzionare la mia famiglia, nello specifico Eleonora, per l'aiuto che mi hanno dato.

Ringrazio poi le persone che il test beam mi ha permesso di conoscere, Fabio e i gruppi del CEA di Saclay e del LPNHE.